SiaABCD – A threonine phosphorylation pathway that controls biofilm formation in *Pseudomonas aeruginosa*

Wee-Han Poh[2‡], Jianqing Lin[5,7‡], Brendan Colley[3a], Nicolai Müller[4], Boon Chong Goh[7,8], David Schleheck[4], Andreas Marquardt[4], Yang Liang[2,5], Staffan Kjelleberg[2,3,5], Julien Lescar[5,7]*, Scott A. Rice[2,5,6]* and Janosch Klebensberger[1]*

‡ These authors contributed equally to the work

* Correspondence: janosch.klebensberger@itb.uni-stuttgart.de, rscott@ntu.edu.sg, julien@ntu.edu.sg

[1]University of Stuttgart, Institute of Biochemistry and Technical Biochemistry, Stuttgart, Germany

[2]Singapore Centre for Environmental Life Sciences Engineering, Nanyang Technological University, Singapore

[3]Centre for Marine Bio-Innovation, School of Biotechnology and Biomolecular Sciences, University of New South Wales, Sydney, New South Wales, Australia ([a]present address: Bio Molecular Systems, Sydney, Australia)

[4] Konstanz Research School Chemical Biology, Departments of Chemistry and Biology, University of Konstanz, D-78464 Konstanz, Germany

[5]The School of Biological Sciences, Nanyang Technological University, Singapore

[6] the ithree Institute, The University of Technology Sydney, Sydney Australia

[7]NTU Institute of Structural Biology, Nanyang Technological University, Singapore

[8] Antimicrobial Resistance Interdisciplinary Research Group, Singapore-MIT Alliance for Research and Technology, Singapore

Running title: The SiaABCD partner switch controls biofilm formation

Keywords: Signalling, Cell aggregation, Biofilms, PP2C, Protein kinase, SiaA, SiaB, SiaC, SiaD, c-di-GMP, *Pseudomonas aeruginosa*, Protein Phosphorylation, threonine phosphorylation pathway, protein-protein interactions, crystal structures, biofilm interference

Abstract

The looming antibiotic crisis and the critical role of biofilms in chronic infections call for novel and tailor-made anti-infective strategies. We previously characterised the PP2C-like phosphatase SiaA and the di-guanylate cyclase SiaD control the formation of macroscopic, suspended biofilms of *P. aeruginosa* cells in response to surfactant stress. We now demonstrate that this regulation is also important for cellular aggregation in response to carbon availability and provide compelling evidence that the SiaABCD pathway functions trough a partner switch mechanism. Our study reveals that SiaA and SiaB represent a threonine-specific protein phosphatase/kinase switch regulating cellular aggregation by balancing the phosphorylation status of SiaC. From these data, we hypothesize that fine-tuning cellular aggregation through SiaABCD constitutes a general strategy used by *P. aeruginosa* to adapt to various environmental conditions and that this pathway represents a novel and promising target for the development of anti-infective drugs against this aggressive opportunistic pathogen.

Introduction

Biofilms are ubiquitous, multicellular structures embedded in a self-made matrix, that can occur attached to a solid surface, floating at the gas-liquid interface as a pellicle and can be freely suspended in the liquid phase as aggregates or flocs[1–3]. The ability to form and disperse from biofilms is a ubiquitous feature of microorganisms and is achieved by differential regulation and production of extracellular polymeric substances (EPS) such as polysaccharides, eDNA and proteinaceous surface adhesins[4–6].

Matrix embedded aggregated cells embedded in biofilms are well known for their increased robustness under stressful environmental conditions compared to their single-cell, planktonic counterparts, which largely explains the evolutionary success of the biofilm lifestyle[7–11]. It is thus not surprising, that biofilm formation can be triggered as an adaptive response to oxidative and nitrosative stress[12,13] and to the presence of toxic compounds such as antibiotics[14,15], surfactants[16,17] or primary fermentation products[18,19]. As a consequence, biofilms enable bacteria to survive in health-care settings despite the use of stringent hygiene regimes[20–22] and to establish chronic infections despite the host immune system and therapeutic interventions[23–28]. Chronic infections are particularly problematic, as they are almost impossible to eradicate with conventional therapies[29–32].

The regulation of biofilm development and virulence traits is complex and can include multiple, highly interconnected, signal transduction pathways[33,6,34–37]. In addition to quorum sensing (QS)[38,39], nucleotide-based second messengers and changes in protein phosphorylation represent key mechanisms for the regulation of these physiological changes[40–43]. Protein phosphorylation is most often mediated by two-component systems (TCSs) or chemosensory signalling pathways[44–46]. TCSs are typically composed of a sensor kinase and a cognate response regulator that elicits a specific response upon its phosphorylation. Most sensor kinases in bacteria belong to the family of histidine kinases, transferring a phosphoryl group from a conserved histidine of its transmitter domain to a specific aspartate residue in the receiver domain of the corresponding response regulator. This type of aspartate phosphorylation is labile and, thus,

61 specific phosphatases are usually not required to inactivate the response over time. In contrast,
62 phosphorylation of a serine or threonine residue are much more stable and, thus, require the additional
63 presence of a phosphatase to facilitate reversible regulation[47,48].

64 *Pseudomonas aeruginosa,* an opportunistic human pathogen of critical concern, is often highly resistant
65 to antimicrobial therapies. It is an ubiquitous organism that can thrive in multiple environmental niches
66 and genetic evidence indicates that infections usually arise from environmental sources[49–52]. Various
67 regulatory pathways affect its biofilm formation and virulence traits, many of which are based on protein
68 phosphorylation including, but not limited to, the GacS/GacA system, the threonine phosphorylation
69 pathway (TPP) and the Wsp, Yfie or HptB pathways[24,53–58]. While *P. aeruginosa* does not generally infect
70 healthy humans, it is a serious threat in hospital environments, particularly for individuals with large burn
71 wounds or chronic diseases such as obstructive pulmonary disease (COPD) and the genetic disorder cystic
72 fibrosis (CF)[29,59–63]. In addition to surface attached biofilms, suspended biofilms of *P. aeruginosa* (i.e.
73 cellular aggregates) have been characterised first for growth under laboratory conditions[28,64]. Notably,
74 such cellular aggregates are also regularly found in chronic infections *in vivo*[26,27,65–67]. Moreover,
75 suspended biofilms greatly influence the development, structure and function of their surface-attached
76 counterparts and have thus been suggested to play an important role in niche colonisation and the chronic
77 manifestation of infections[68,69].

78 We previously demonstrated that SiaA and the di-guanylate cyclase (DGC) SiaD regulate the formation of
79 large, macroscopic, DNA-containing suspended biofilms in response to the toxic surfactant sodium
80 dodecyl sulfate (SDS) in a c-di-GMP-dependent manner[16,70–72]. We now report that all genes encoded in
81 the *siaABCD* operon are also involved regulation of the cellular aggregation in response to carbon
82 availability including the previously described formation of suspended biofilms during growth on
83 glucose[64]. We demonstrate that the phosphorylation status of the SiaC protein at position threonine 68
84 (T68) is crucial for this regulation and that SiaC is a substrate for the threonine-specific protein

85 phosphatase SiaA and its kinase counterpart SiaB. We further report crystal structures of the protein-
86 phosphatase family-2C (PP2C) domain of SiaA and of the SiaC protein providing insights into their catalytic
87 mechanism and interaction. Our results strongly suggest that the SiaABCD pathway functions through a
88 partner switch mechanism, in which SiaC controls cellular aggregation by regulating SiaD activity, most
89 likely through direct protein-protein interaction. It further highlights the importance of this pathway in
90 the adaptation of *P. aeruginosa* to variable environmental conditions. We hypothesise that the regulation
91 of biofilm formation through SiaABCD plays an important role in the colonisation of new niches/habitats
92 and supports the persistence of cells under unfavourable conditions.

93 ## Results

94 ***SiaABCD is involved in biofilm formation during growth on SDS and glucose***

95 Cells of *P. aeruginosa* preferentially grow as suspended biofilms in minimal medium with glucose
96 (aggregates up to 400 µm in size) or SDS (macroscopic aggregates in the mm range)[16,64]. To investigate
97 whether all genes of the *siaABCD* operon[70] are involved in biofilm formation under these conditions, we
98 tested growth of individual mutant strains in microtiter plates (**Figure 1AB**).

99 As shown previously, growth on SDS led to the formation of macroscopic aggregates in the parental strain
100 but not in the Δ*siaA* and Δ*siaD* mutants[70]. Likewise, no macroscopic aggregates were observed in cultures
101 of Δ*siaC*, whereas Δ*siaB* showed increased aggregation. The aggregation was inversely correlated with the
102 optical density (OD_{600}) of the surrounding medium: the OD_{600} in cultures of strains Δ*siaA*, Δ*siaC* and Δ*siaD*
103 was higher (darker colour in normalised pictures; **Figure 1B**) than that of the parental strain and the Δ*siaB*
104 mutant. No macroscopic aggregates were found during growth with glucose for all strains. However, the
105 OD_{600} of the culture medium followed a similar pattern as for those grown on SDS. We therefore
106 quantified the attached biofilms in glucose cultures (**Figure 1C**). The parental strain formed significantly
107 more biofilm (2.3 - 2.8 fold) compared to Δ*siaA*, Δ*siaC* and Δ*siaD* mutants after 15 h. In contrast,
108 inactivation of *siaB* strongly increased biofilm formation by 16.2 fold. Overall, these results revealed that
109 attached biofilm formation during growth on glucose follows the same pattern as the formation of
110 suspended aggregation observed for cultures grown on SDS.

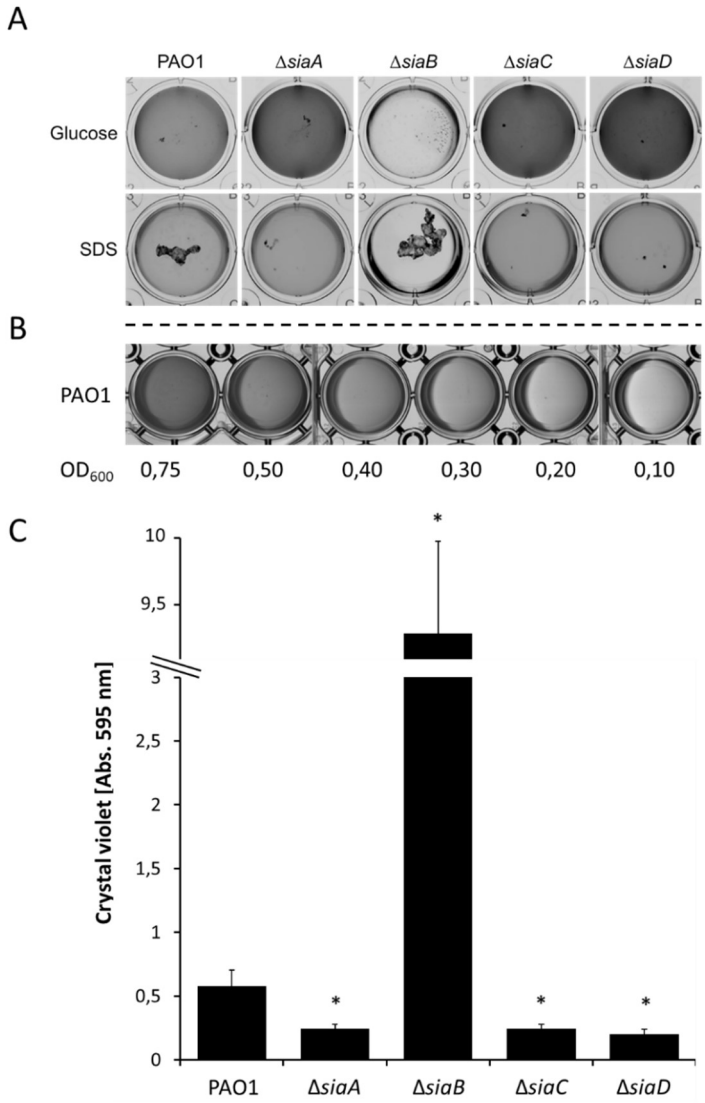

Figure 1: **(A)** Growth of the *P. aeruginosa* strains on 22 mM glucose or 3.5 mM SDS in 12 well microtiter plates after 18 h, 30°C, and shaking at 200 rpm. Images were acquired using a flat-bed scanner (Umax Powerlook), normalised by the "match colour" function of Photoshop (Adobe Photoshop CS5), and converted to greyscale. **(B)** Images of different OD_{600} derived from a serial diluted culture of the parental strain grown on glucose. **(C)** Quantification of attached biomass using a crystal violet (CV) staining assay after growth with glucose for 15 h at 30°C and shaking at 200 rpm. Data are presented as the mean value of four biological replicates and the error bar represents the corresponding standard deviation. Statistical differences between strains are indicated (*$p < 0.003$, *$p < 0.009$) and were calculated using a two-sided, unpaired student *t*-test ($\alpha = 0.05$, $n = 4$).

SiaABCD regulates the ratio of freely suspended cells and cells residing in cellular aggregates

Scanning electron microscopy (SEM) (**Figure 2**) confirmed individual single cells as well as densely packed, multicellular aggregates (*white arrows*) in cultures of the parental strain, even at lower magnification (1,300×; left panel of pictures); imaging at higher magnification (10,000×; right panels) showed that the multicellular aggregates of different sizes are arranged as three-dimensional structures that projected

118 above the substratum. These multicellular aggregates were observed also for the Δ*siaA*, Δ*siaC* and Δ*siaD*
119 mutants at lower magnification (1,300×), but their abundance was noticeably lower than for the parental
120 strain. Higher magnification (10,000×) showed that these areas were less structured in those mutant
121 strains compared to the parental strain. However, the Δ*siaB* mutant formed much larger, much more
122 densely packed aggregates than the parental strain. Light diffraction analysis (LDA) can be used to
123 determine the size distribution of aggregates in liquid cultures[64] and a corresponding analysis in our
124 present study demonstrated that cultures of the parental strain were dominated by 10 – 200 µM particles
125 (≥ 77% of the total bio-volume of all particles). Particles < 10 µm, which include the single cells,
126 represented only a minor fraction (≤ 4%) and particles >200 µm were present in both biological replicates
127 (7% – 28%). In line with SEM results, the distribution of particles in cultures of the Δ*siaA*, Δ*siaC* and Δ*siaD*
128 mutants were strongly shifted towards smaller sizes. We consistently observed a substantial decrease in
129 the number of particles >200 µm and a concomitant increase in the bio-volume of particles <10 um for
130 Δ*siaA* (≥ 8.4 fold), Δ*siaC* (≥ 15 fold) and Δ*siaD* (≥ 10.8 fold). In contrast, cultures of Δ*siaB* were dominated
131 by particles >200 µm (≥ 77%) and almost no particles < 10 µm were detected (≥ 1%).

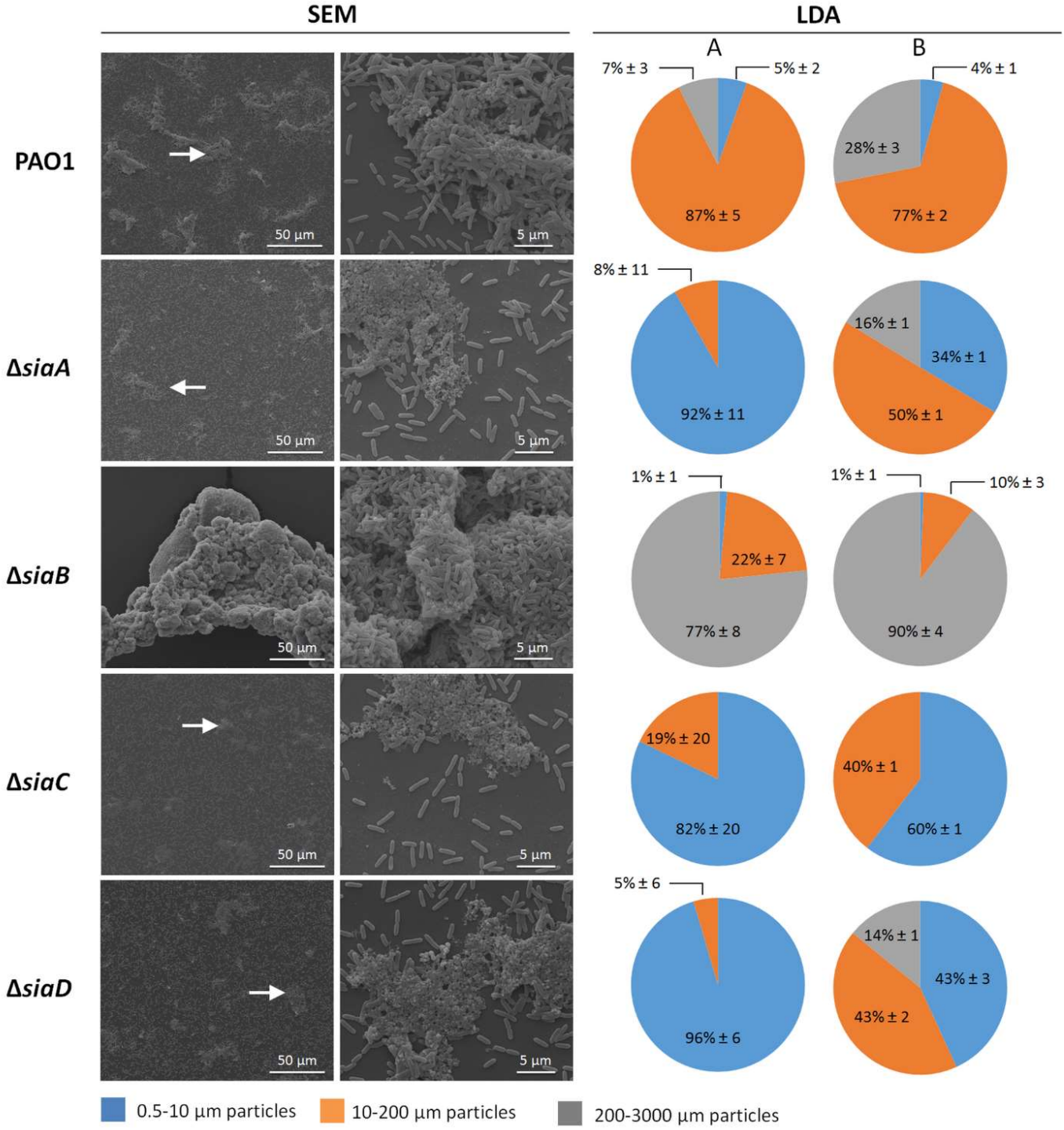

Figure 2: Scanning electron microscopy (SEM) and laser diffraction analysis (LDA) demonstrated the different aggregation phenotypes of *P. aeruginosa* wildtype and mutant strains during growth with glucose. Triplicate cultures of strains were grown with 22 mM glucose in 50 mL cultures shaking at 200 rpm at 30°C. After 5.5 h incubation, the replicate samples were pooled and used for SEM. The white arrows (left panel) highlight representative regions showing aggregated cells, which were then examined at higher magnification (right panel). The samples were also analyzed using a particle size analyzer (SALD 3101, Shimadzu; see Material and Methods) in the range 0.5 - 3000 µm diameter. The data obtained from two independent replicates (A and B) is presented as percentages of the total bio-volume of particles distributed over three different size ranges (single cells, microscopic aggregates and macroscopic aggregates) relative to the total bio-volume of all particles detected. The data are the mean value of triplicate measurements with the corresponding technical error (see Supplementary for details).

134 ***SiaABCD regulates biofilm formation as a response to carbon availability***

135 Biofilm formation is a dynamic process that varies according to the time point of sampling and the carbon
136 source used. Thus, we monitored the impact of the SiaABCD pathway during biofilm development and on
137 growth with various carbon sources (**Figure 3, Figure S1**). In these experiments, the parental strain always
138 exhibited the same growth pattern, irrespective of the carbon source used: *i)* a steady increase in biofilm
139 formation while the carbon source was in excess; *ii)* a decrease in biofilm formation upon exhaustion of
140 the carbon source; and *iii)* an increase in optical density in the culture supernatant that lagged behind
141 biofilm formation, but continued to increase even after the cells experienced carbon starvation.

142 The Δ*siaA* (**Figure 3**), Δ*siaC* (**Figure S1**) and Δ*siaD* (**Figure S1**) mutants showed a similar growth pattern,
143 however, with a strong decrease in biofilm formation and mild increase in the maximal OD_{600} at the end
144 of the experiment. In contrast, the Δ*siaB* mutant predominantly grew as a biofilm with generally lower
145 planktonic growth compared to all other strains. Biofilms of Δ*siaB* dispersed upon glucose and succinate
146 limitation, but not when grown on ethanol or 2,3-butanediol. However, it is important to note that
147 cultures of the parental strain, Δ*siaB* and Δ*siaC* growing on 2,3-butanediol were still not carbon-limited
148 by the end of the experiment (< 0.6 mM). In contrast, carbon depletion and dispersal was observed for all
149 other strains and conditions.

150

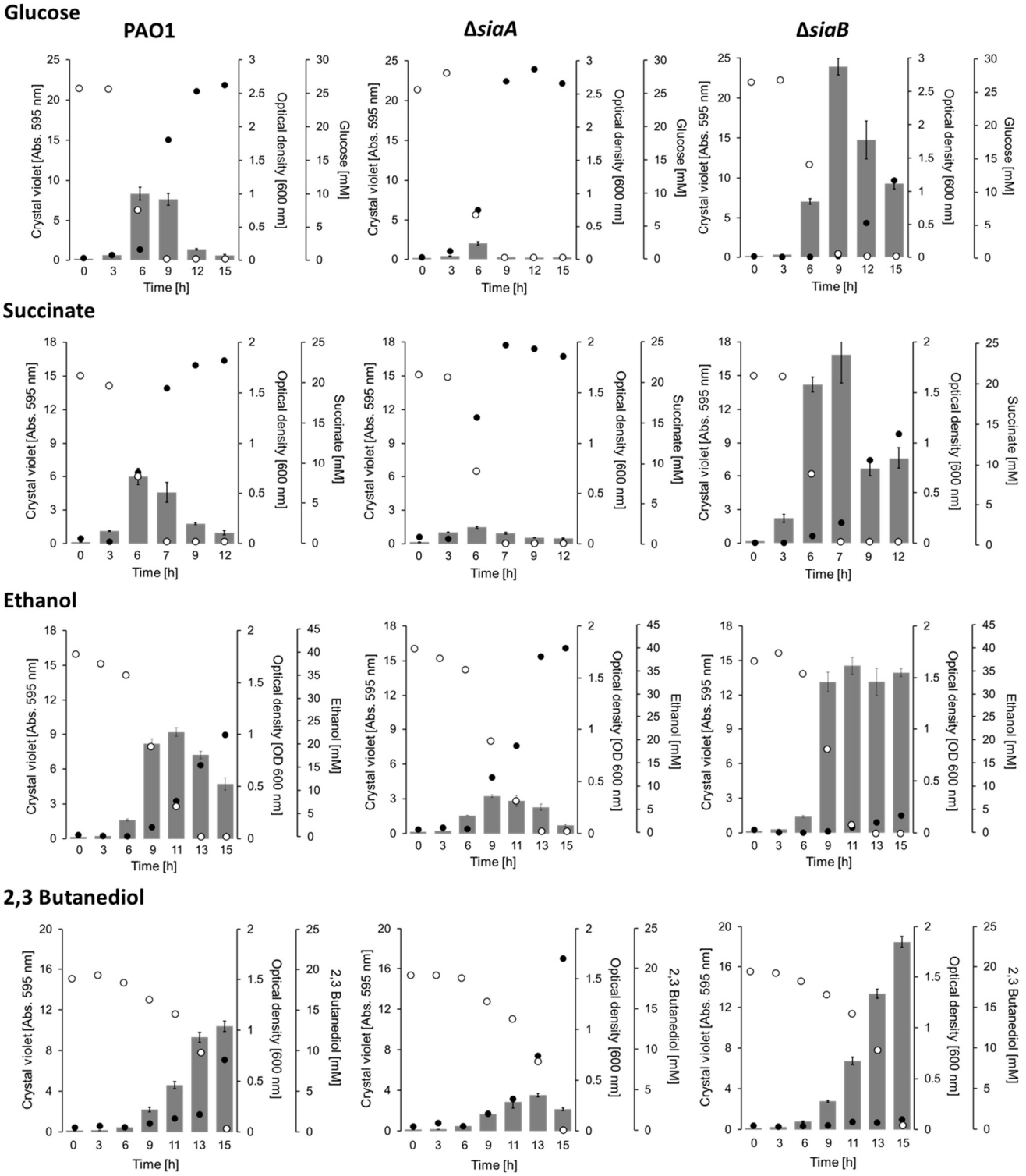

151

Figure 3: Quantification of formation of attached biofilms and of growth in suspension by the *P. aeruginosa* strains, as followed in liquid cultures grown with 22 mM glucose, 20 mM succinate, 40 mM ethanol or 20 mM 2,3-butanediol. Individual 24 well microtiter plates were used to quantify attached biofilms by crystal violet (CV) staining (*grey bars*) as well as the growth in the supernatant as OD_{600} (*black dots*); substrate concentrations were also determined (*open circles*). For crystal violet (CV) staining, the error bars represent the standard deviation of four biological replicates. The data of OD_{600} and substrate concentration represent the mean value from the same quadruplicates but quantified from pooled (1:1:1:1 [v/v/v/v]) samples using a photometer, the GO assay kit and specific HPLC methods, respectively (see Methods section for details). Cultures were incubated at 30°C and 200 rpm shaking.

152

153

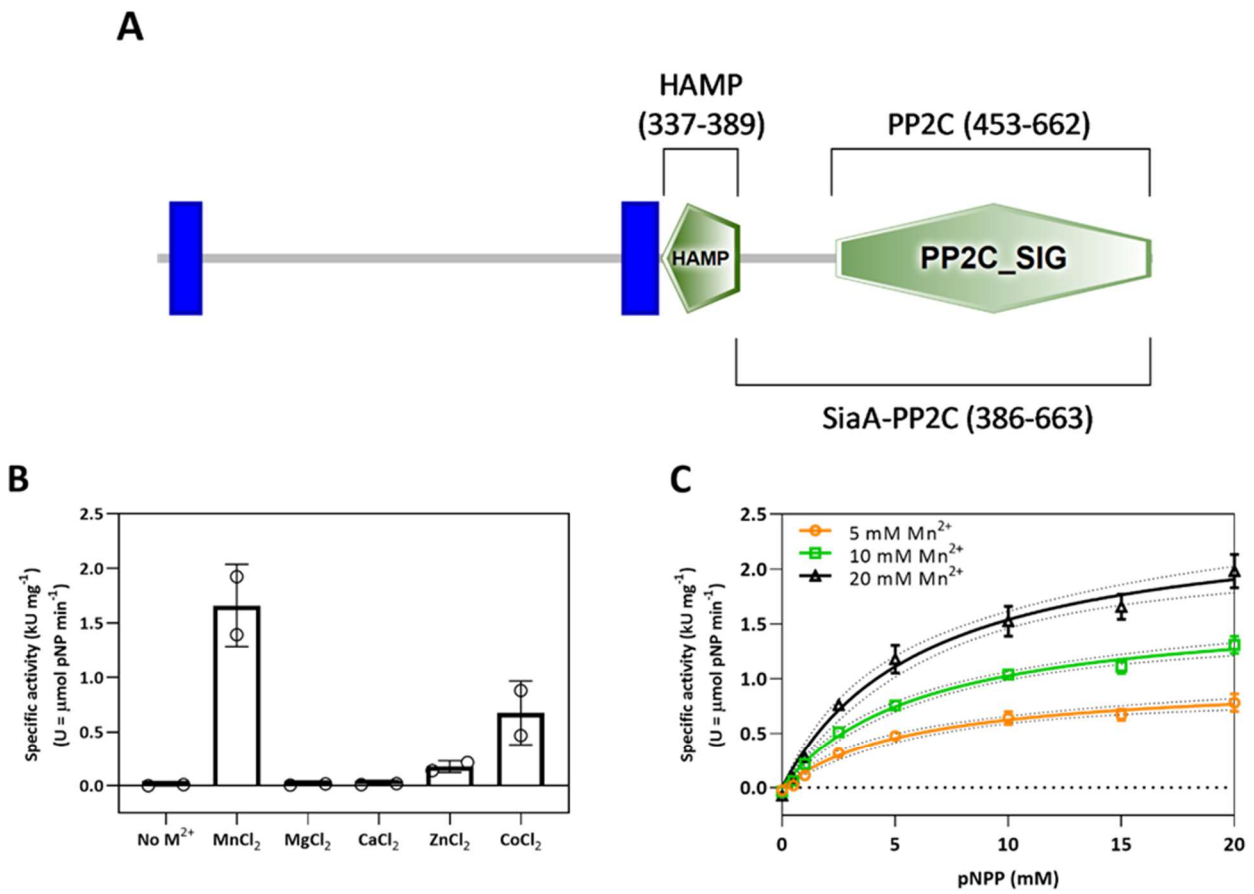

D

Mn^{2+} (mM)	V_{max} (kU mg^{-1})	K_m (mM pNPP)	k_{cat} (min^{-1})
5	0.9968 ± 0.06263	5.943 ± 1.004	3.345 ± 0.2104
10	1.66 ± 0.07342	6.161 ± 0.722	5.572 ± 0.246
20	2.5 ± 1.01	6.254 ± 1.01	8.389 ± 0.5142

154

Figure 4: Biochemical characterization of the purified phosphatase activity of the C-terminal part (SiaA-PP2C; amino acids 386-663) of the SiaA protein (Genbank: NP_248862) with p-nitrophenyl phosphate (pNPP) as substrate. Phosphatase activity was measured as increase in absorbance at 405 nm. Absorbance readings were converted to µM production formation using a generated standard curve for the determination of specific activities. The buffer used contained 150 mM NaCl, 20 mM Tris-HCl pH 7.5 and incubations were performed at 37°C. For enzyme kinetics, a higher buffering capacity of 100 mM Tris-HCl pH 7.5 was used. **(A)** Representation of the SiaA protein using the SMART online tool (http://smart.embl-heidelberg.de/). The amino-acid range of the predicted PP2C_SIG and HAMP domains as well as of the SiaA-PP2C fragment are indicated. **B)** Specific activities of SiaA-PP2C in the presence of various metal ions (20 mM) were measured using 10 mM pNPP. Data are shown as the mean value (*black bars*) of duplicate measurements (*white dots*). **(C)** Michaelis-Menten plots showing the specific activities of the purified SiaA-PP2C with various concentrations pNPP and Mn^{2+}. **(D)** The maximum velocities (V_{max}), substrate affinities (K_M), and turnover number (k_{cat}) were derived from the data in **(C)** by nonlinear regression to a Michaelis-Menten model and are presented as best-fit values.

155

156 ***SiaA shows Mn^{2+}-dependent phosphatase activity with pNPP***

157 The SiaA protein is predicted to be a PP2C-like protein phosphatase (PPM-type)
158 (http://www.pseudomonas.com/feature/show/?id=103077&view=functions). A distinctive feature of
159 these phosphatases is their dependency on Mn^{2+} or Mg^{2+} ions as cofactors and serine and/or threonine
160 residues in their target protein (http://www.ebi.ac.uk/interpro/entry/IPR001932). To characterize the
161 activity of the SiaA protein, we purified the C-terminal part of SiaA (amino acids 386-663; SiaA-PP2C;
162 Genbank: NP_248862) including the putative PP2C-like phosphatase domain (amino acids 453-662) from
163 the parental strain using *Escherichia coli* as a heterologous host by metal-affinity chromatography (**Figure**
164 **4A**; **Figure S2**). The activity of the purified SiaA-PP2C was tested for its metal dependency using p-
165 nitrophenyl phosphate (pNPP). SiaA-PP2C showed strong phosphatase activity in the presence of 20 mM
166 of Mn^{2+} (1.658 ± 0.3766 kU mg^{-1}), lower activity in the presence of 20 mM Co^{2+} (0.6747 ± 0.2932 kU mg^{-1})
167 and no detectable activity with similar amounts of Mg^{2+}, Ca^{2+} or Zn^{2+} (**Figure 4B**). Subsequently, kinetic
168 parameters for SiaA-PP2C at various Mn^{2+} concentrations were derived from nonlinear regression to a
169 Michaelis–Menten model (**Figure 4C, Table 4E**). From experiments with 20 mM Mn^{2+}, a maximum velocity
170 of (V_{max}) of ~2.5 ± 1.01 kU mg^{-1}, a substrate affinity (K_M) of ~6.254 ± 1.01 mM and a turnover number
171 (k_{cat}) of ~8.389 ± 0.5142 min^{-1} were calculated..

172 ***SiaA is a Ser/Thr phosphatase that uses phosphorylated threonine residue 68 of SiaC as substrate***

173 SiaC contains a phosphorylation site at threonine residue 68 (T68)[73]. To confirm this phosphorylation site
174 and to test whether it represents a substrate for the phosphatase domain SiaA-PP2C and the predicted
175 kinase SiaB (see section below), His6-tagged SiaC variants were purified from *E. coli* and Δ*siaA* cell lysates
176 (**Figure S2**) and analysed by shotgun peptide-mass spectrometry (PMS). For the SiaC variant purified from
177 *E. coli*, the T68-containing peptide (peptide [LLYLN**T**SSIK]) was identified predominantly by fragment-
178 masses derived of precursor ions of the parental, non-phosphorylated peptide and only at > 1000 fold
179 lower intensity (1.4×10^{11} vs. 4.0×10^{14} peak area) by precursor ions of its phosphorylated analogue;
180 hence, these preparations contained almost exclusively non-phosphorylated protein.

181 For the purified *P. aeruginosa* SiaC ($SiaC^P$) variant however, the corresponding phosphorylated peptide
182 was found at a higher abundance than the non-phosphorylated peptide (7.8 x × 10^6 vs. 3.2 × 10^6 peak
183 area). Hence, these preparations contained relevant amounts of phosphorylated $SiaC^P$ (71.27% of total
184 peak area). The $SiaC^P$ preparations was tested as substrates for SiaA-PP2C and incubation, the protein
185 samples were separated by SDS-PAGE and the protein band representing the SiaC protein were excised
186 and analysed by PMS (**Figure 5A; Tables 3**). Incubation with SiaA-PP2C resulted in > 10 fold increase in the
187 phosphorylated peptide (LLYLN**T**SSIK) compared to the control incubation without SiaA-PP2C added.
188 Hence, the PMS data obtained from these enzyme assays provide direct evidence that the phosphorylated
189 threonine at position 68 of SiaC is a target for SiaA phosphatase activity.

190 ***SiaB is a protein kinase that uses dephosphorylated SiaC as a substrate***

191 Protein sequence analysis of SiaB (**Figure 5B**) suggested that SiaB is a protein kinase. To test whether SiaC
192 is a target for SiaB activity, we purified a His6-tagged allele of SiaB from *E. coli* by metal-affinity
193 chromatography (**Figure S2**) and performed ATP consumption assays (ADP-Glo™ Kinase Assay; Promega)
194 with SiaC as the substrate (**Figure 5C**). Incubation of SiaB (0.5 µM) alone or with $SiaC^P$ (5 µM) did not
195 consume ATP, whereas incubations of SiaB with SiaC (5 µM) consumed 4.45 µM ATP.

196 To confirm that SiaB was specific towards position T68 of the SiaC protein, we performed the kinase assay
197 in the absence or presence of ATP and subsequently analysed the SiaC protein by PMS (**Figure 5A; Tables**
198 **S3**). For SiaC incubations with SiaB in the absence of ATP, the non-phosphorylated peptide was > 1000
199 fold more abundant than the corresponding phosphorylated peptide (2.9 x 10^9 vs. 1.3 x 10^6 peak area).
200 Following incubation of SiaC with SiaB in the presence of ATP, the abundance of the phosphorylated
201 peptide increased (1.5 x 10^9 peak area) and the non-phosphorylated peptide decreased dramatically (2.7
202 x 10^8 peak area), demonstrating that T68 of SiaC constitutes a target for SiaB kinase activity.

A

Incubation	precursor ion matches for peptide [LLYLNTSSIK]	Peak area	PSMs
SiaC^P – SiaA-PP2C	non-phosphorylated	1.9 x 10^9	95
	phosphorylated	1.8 x 10^8	34
SiaC^P + SiaA-PP2C	non-phosphorylated	3.7 x 10^9	178
	phosphorylated	1.6 x 10^7	7
SiaC + SiaB - ATP	non-phosphorylated	2.9 x 10^9	135
	phosphorylated	1.3 x 10^6	4
SiaC + SiaB + ATP	non-phosphorylated	2.7 x 10^8	30
	phosphorylated	1.5 x 10^9	91

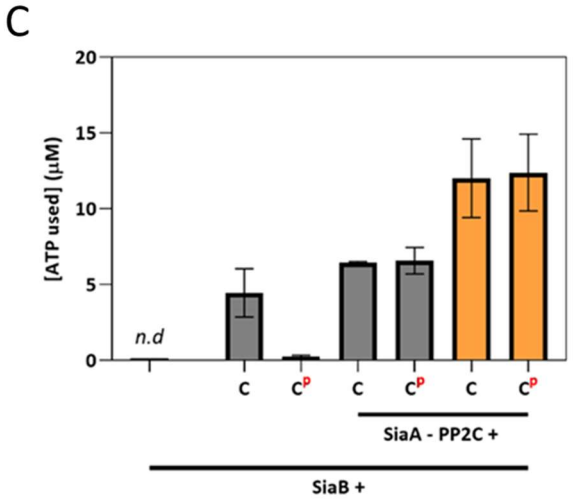

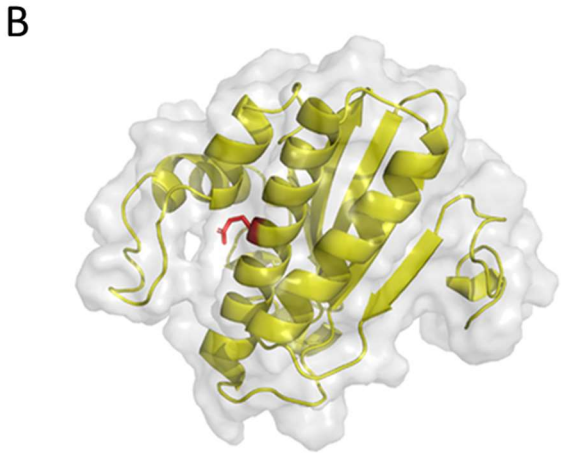

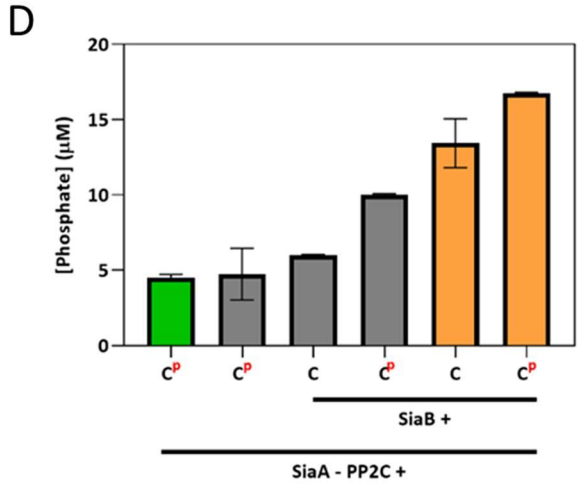

203

Figure 5: (A) Summary of shotgun peptide-mass spectrometry (PMS) results from analysis of phosphorylated SiaC^P and non-phosphorylated SiaC after incubation with the phosphatase domain of SiaA (SiaA-PP2C) and the predicted SiaC-kinase SiaB, respectively. The relative abundances of the SiaC peptides containing the phosphorylation site (threonine [T68] in peptide [LLYLN**T**SSIK]) as identified by their parental (and by their fragment) masses without or with mass-shift from T68-phosphorylation, are indicated as peak area and number of peptide spectrum matches (PSMs). All incubations were performed in suitable buffer conditions for 2 h at 30°C and then separated by SDS-PAGE for PMS (see Supplementary file for details) **(B)** Homology model (C-score = -2.36, estimated TM-score = 0.44 ± 0.14 and estimated root-mean-square-mean (RMSD) = 10.4 ± 4.6 Å) of SiaB (PA0171) predicted using I-Tasser (https://zhanglab.ccmb.med.umich.edu/I-TASSER/) shown as cartoon with 80% transparent surface using the Pymol software (version 2.1.1). The predicted catalytic glutamic acid residue at position 61 of the putative protein kinase is highlighted (*red sticks*). **(C)** ATP consumption of SiaB kinase activity measured by the ADP-Glo™ assay kit. Assays were performed in the presence of 10 µM or 25 µM (*orange bars*) ATP. **(D)** Phosphate released via SiaA phosphatase activity as measured by the malachite green assay. All reactions were carried out with 0.5 µM SiaA or B with 5 µM SiaC in buffer containing 20 mM $MgCl_2$ or $MnCl_2$ (*green bar*), and 10 or 25 µM ATP (*orange bars*). Data represent results from at least two independent replicates and error bars represent standard deviation of the mean. Results below the detection limit are indicated (*n.d.*).

204

205 Notably, reactions in which SiaB and SiaC or SiaC^P were incubated together with SiaA-PP2C (0.5 µM), the

206 consumption of ATP was increased (6.42 µM and 6.57 µM in the presence of 10 µM ATP and to 12.01 µM

207 and 12.39 μM in the presence of 25 μM of ATP, respectively) when observed after the reactions (**Figure**
208 **5C**). These experiments demonstrated that SiaA-PP2C was functional in the presence of Mg^{2+} and that
209 SiaA-PP2C and SiaB were both enzymatically active on their respective substrates ($SiaC^P$ and SiaC,
210 respectively), catalysing a cycle of SiaC phosphorylation and de-phosphorylation. Activity of SiaA with
211 Mg^{2+} ions was not observed with the artificial substrate pNPP (**Figure 4A**). To test whether the metal-
212 dependency of SiaA-PP2C is different using $SiaC^P$ as substrate compared to pNPP, we quantified activities
213 using a Malachite-Green phosphate assay (**Figure 5D**). In reactions containing SiaA-PP2C and $SiaC^P$, the
214 concentration of phosphate quantified in the presence of Mg^{2+} (4.74 μM) was slightly higher than that
215 determined in the presence of Mn^{2+} (4.52 μM), and both were strongly correlated with the amount of
216 $SiaC^P$ (5 μM) added. In samples containing SiaA-PP2C, SiaB, and SiaC or $SiaC^P$ in the presence of Mg^{2+} ions
217 and 25 μM ATP, much higher phosphate concentrations were detected (13.44 μM and 16.76 μM,
218 respectively), which in addition did not correlate with the amount of SiaC added. Thus, these experiments
219 revealed that SiaA can utilise both Mg^{2+} and Mn^{2+} ions as metal cofactors.

220 ***Crystal structure of the PP2C domain of SiaA reveals a homodimer***

221 The structure of the PP2C domain of SiaA (SiaA-PP2C) in the presence of Mg^{2+} ions at the active site was
222 determined. Native crystals of SiaA-PP2C were obtained in conditions Morpheus A11 (Molecular
223 Dimensions), with space group of $P2_12_12_1$ that diffracted to a resolution of 2.1 Å. Phases were obtained
224 using single-wavelength anomalous dispersion (SAD) with a single SeMet derivative crystal. Statistics of
225 the data collection, structure determination and refinement are displayed in **Table S4**.

226 The SiaA-PP2C domain is arranged as a tight dimer in the crystal asymmetric unit. The electron density
227 map of SiaA-PP2C allowed unambiguous tracing of residues 407 to 663 for monomer A and 409 to 663 for
228 monomer B. However, no clear electron density was present for residues 521-528 and 578-581 of chain
229 A and residues 522-527 and 577-579 of chain B, indicating a high degree of flexibility in these solvent-

230 exposed loops regions. The SiaA-PP2C monomer adopts the canonical α–β–β–α fold first described for

231 the human PP2C[74] and subsequently found in several other phosphatases[75,76] (**Figure 6A**).

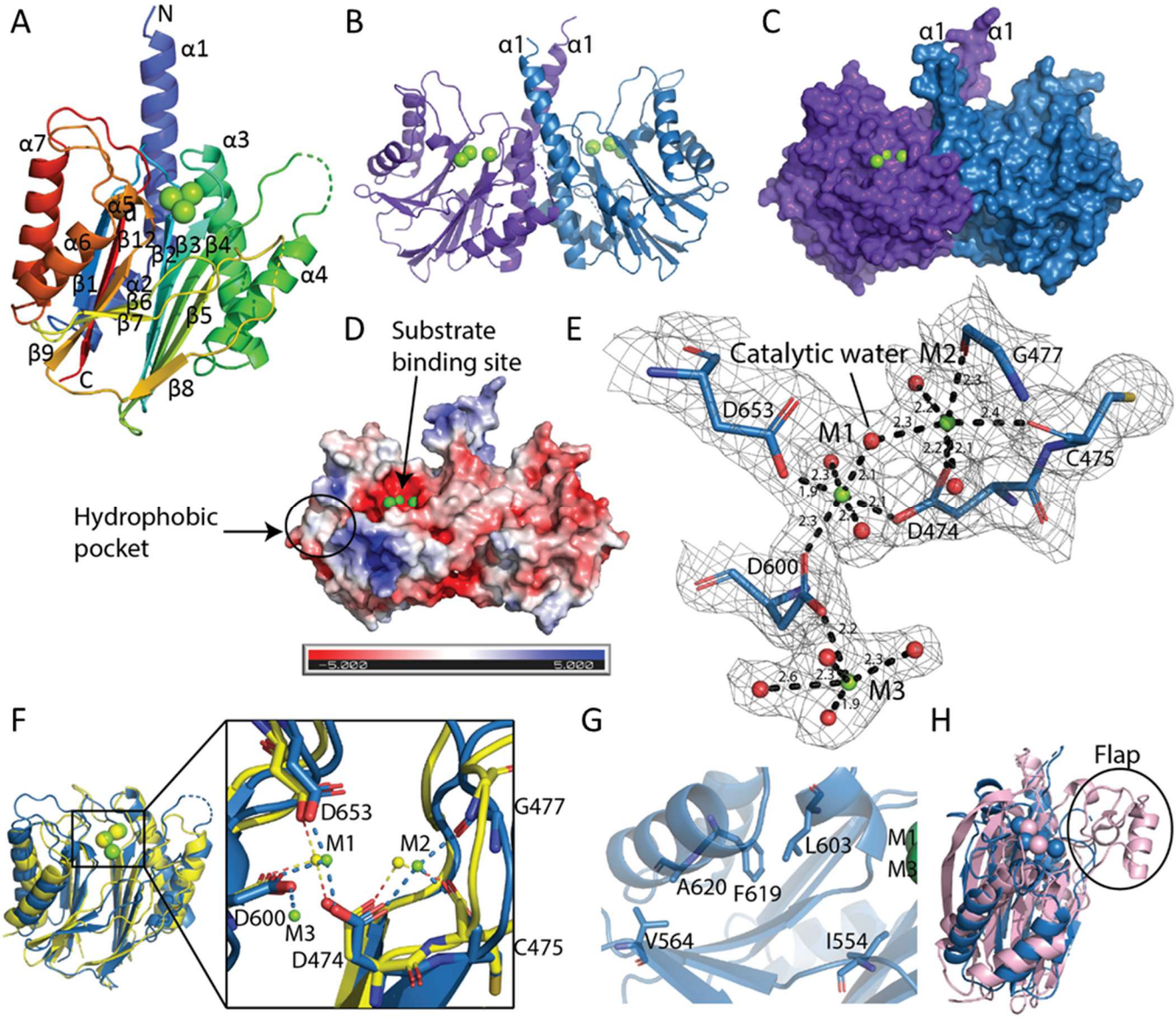

232

Figure 6: The SiaA-PP2C structure. **(A)** "Rainbow" representation of the SiaA-PP2C monomer. The N-terminus of SiaA-PP2C is coloured in blue and the C-terminus in red, with secondary structures labelled. The three Mg^{2+} ions identified at the active site are represented as green spheres. **(B)** The SiaA-PP2C dimer. Monomer A is in purple and B in blue. **(C)** Surface representation of the SiaA-PP2C dimer using the same colour code, highlighting the extensive interface stabilizing the dimer. **(D)** Surface electrostatic potential of SiaA-PP2C homodimer in the same orientation as in panel C. **(E)** Close-up view of the active site of the PP2C-like phosphatase domain of SiaA-PP2C with conserved acidic residues in the active site shown as sticks and labelled. An electron density map with Fourier coefficients $2F_O$-F_C is overlaid at a level of 1σ above the mean. The Mg^{2+} ions are shown as green spheres and the oxygen atoms of the coordinating water molecules are displayed as red spheres. M1 and M2 are both coordinated by oxygen atoms from three residues and three water molecules in an octahedral manner. Distances between the metal ions and the coordinating atoms are indicated. **(F)** Overlay of SiaA_PP2C monomer B (blue) and the phosphatase domain of Rv1364C (yellow). Mg^{2+} ions M1 and M2 of SiaA-PP2C shown as green spheres overlap with Mn^{2+} ions of Rv1643C (yellow spheres). The α1 and α2 helices of SiaA-PP2C are not displayed for clarity. **(inset)** Magnified view of the active site. Metal coordinating residues of SiaA-PP2C are labelled. **(G)** Residues of the hydrophobic pocket shown as sticks. **(H)** Superposition of SiaA monomer B (blue) and human PPM1A (light pink; PDB code 6B67-A). The Flap sub-domain of human PPM1A (absent in SiaA-PP2C) is circled.

233

234 The core structure of the SiaA-PP2C monomer is a β-sandwich composed of two antiparallel β-sheets each
235 comprising five β-strands. The active site is at the apex of the β sheet structure (**Figure 6B**). This core
236 structure is flanked on the N-terminal side by helices α1-α4 and on the C-terminal end by helices α5-α7,
237 forming a four-layered αββα structure. The two monomers interact extensively with each other through
238 residues projecting from helices α1, α2 and α3, forming a compact homodimer that buries a total solvent
239 accessible area of 1392 $Å^2$ (**Figure 6B** and **C**), which is consistent with the observation of a dimer by size
240 exclusion chromatography (data not shown). The homodimer presents two concave surfaces that are
241 likely to accommodate the incoming substrates (**Figure 6D)**.

242 An automated search using the Dali server (ekhidna2.biocenter.helsinki.fi/dali) of 3D structures similar to
243 SiaA-PP2C returned PP2C-type phosphatase as top hits (Rv1364C with a Z score of 23.6 and a RMSD of 2.2
244 Å for 210 superimposed α-carbon atoms). Despite a very low overall amino-acid sequence identity (17%),
245 these structures share a conserved fold and several strictly conserved active site residues with SiaA-PP2C:
246 D457, D474, G477, D600, G601 and D653 (**Figure 6E and S3**). A structural comparison of the active site of
247 SiaA-PP2C with the active site of the phosphatase domain of Rv1364C (PDB code: 3KE6) from
248 *Mycobacterium tuberculosis* is shown in **Figure 6F**. The two Mg^{2+} ions labelled as M1 and M2 directly
249 involved in the catalytic mechanism are coordinated by oxygen atoms from three evolutionary conserved
250 aspartate residues and occupy equivalent positions in SiaA-PP2C compared to the two Mn^{2+} ions found in
251 the Rv1364C active site. Metal-coordinating residues are all conserved except C475 of SiaA-PP2C, which
252 interacts with metal ion M2 through its carbonyl oxygen (**Figure 6E and F**). However, compared to
253 Rv1364C, which only has two bound metal ions, a third Mg^{2+} ion (M3) was found in SiaA-PP2C coordinated
254 by D600 and with an incomplete octahedral coordination shell. D604 and D534 assist in stabilization of
255 M3 through formation of hydrogen bond with M3-coordinating water molecules. Given the structural
256 similarity with PP2C[74], an S_N2 mechanism is the most plausible whereby the water molecule bridging M1
257 and M2 (**Figure 6E**) performs a nucleophilic attack of the phosphorus atom from the phosphate bound to

258 the threonine target residue. However, M3 could also play a direct role in the catalytic activity, as was
259 recently proposed for the human PPM1A protein, a negative regulator of cellular stress response
260 pathways[77,78]. We note that near the entrance of the active site, a hydrophobic pocket lined with residues
261 I554, V564, L603, F619 and A620 constitutes an attractive site for the design of inhibitors (**Figure 6D** and
262 **G**). Another distinct feature of SiaA-PP2C is a flexible loop located between β7 and β8, whereas a Flap
263 subdomain, which has been reported to aid in substrate specificity, is present at the equivalent position
264 in human PPM1A and many other PP2C-type phosphatases[78] (**Figure 6H**).

265 ***Crystal structure of SiaC reveals similarity with anti-sigma factor antagonists***

266 Native crystals of SiaC were grown (C6 conditions of the JCSG+ kit from Molecular Dimensions: 0.1 M
267 Phosphate/citrate, pH 4.2, 40% (v/v) PEG 300), with space group I222 and diffracted to a maximum
268 resolution of 1.7 Å. The structure was determined by SAD using SeMet derivative crystals obtained in
269 conditions A9 from Morpheus (Molecular Dimension) (**Table S4**). Clear electron density maps allowed
270 complete tracing except for residues 101-103, which are located in the flexible loop between the α3 helix
271 and β5 strands. The SiaC protein comprises six β-strands arranged in a mixed parallel/antiparallel fashion
272 and three α-helices (**Figure 7A**). A hydrophobic pocket next to T68 is formed by residues L61 and L63
273 projecting from β4, W95 from β5, I71 and M74 from α2, L107 and F111 from α3 while L66 belongs to the
274 β4-β5 loop (**Figure 7B and C**).

275 An automated search of structures similar to SiaC identified the anti-sigma factor antagonist SpoIIAA from
276 *Mycobacterium paratuberculosis* (PDB accession code: 4QTP**; Figure 7D**) as the top hit with a Z score of
277 9.0, an amino-acid sequence identity of 10% and a RSMD of 2.8 Å over the α-carbon atoms of 117 residues.
278 Despite sharing very low sequence identity, a closer examination of both structures reveals a conserved
279 overall topology with several unique features, especially at β3, β4 strands and α3 helix that are longer in
280 SpoIIAA compared to SiaC. These variations are probably related to differences in the ability to establish

281 protein-protein interactions. Nonetheless, their target phosphorylation sites, T68 for SiaC and S58 for
282 SpoIIAA, are both located at the N-terminus of helix α2.

283 To compare the phosphorylated and non-phosphorylated form SiaC, a molecular model was built by
284 adding a phosphate group to T68 (**Figure 7E**). After energy minimization, no major structural difference
285 was observed between the SiaC structure and the predicted $SiaC^P$ structure, except that the N-terminal
286 half of α3 shifts slightly away from the hydrophobic pocket defined above (by distances of 1.2 Å for L107
287 and 1.7 Å for F111). To gain insights into the protein-protein interactions between SiaB and SiaC, we used
288 a homology model of SiaB based on the anti-sigma factor SpoIIAB of *Bacillus stearothemophilus* (PDB
289 accession code: 1L0OA), representing the closest structural homologue with a TM-score of 0.672, RMSD
290 of 2.18 Å, IDENa of 0.130 and Cov of 0.761 (**Figure 5B**). To predict the complex of SiaB and SiaC, the SiaB
291 model and SiaC structure were superimposed to the complex of SpoIIAA and SpoIIAB of *B.*
292 *stearothemophilus* (PDB 1THN), followed by manual adjustment to eliminate clashes and energy
293 minimization[79]. This bioinformatics approach resulted in a probable complex of SiaB/SiaC, in which two
294 molecules of SiaB form a dimer, where each SiaB monomer binds to one SiaC molecule. In this model,
295 residue T68 of SiaC lies next to the putative catalytic base E61 of SiaB (**Figure 7E**). This residue was found
296 to form a hydrogen bond with the substrate hydroxyl group in functionally similar protein kinases, lending
297 support to the proposed model[80,81].

298 Isothermal titration calorimetry (ITC) revealed a dissociation constant (K_d) of 59.4 nM between SiaB and
299 SiaC (**Figure 7G and H**). The binding of the two proteins was driven by both a decrease in enthalpy and
300 increase in entropy. The stoichiometry of 0.5 suggested that only one SiaC molecule binds to a dimer of
301 SiaB. Binding of SiaC to the second SiaB molecule of the dimer was not observed, even when an excess of
302 SiaC was injected (**Figure S4**). In contrast, a 2SiaB:2SiaC complex was suggested by size exclusion
303 chromatography (SEC) when SiaB and SiaC were mixed in equal molar ratio and incubated at room
304 temperature for 1 h (**Figure 7H**). Even though the stoichiometry could not be fully resolved, SEC profile of

SiaB/SiaC mixture with the addition of 10 mM ATP and 20 mM $MgCl_2$ clearly demonstrated dissociation of the SiaB/SiaC complex, most likely as a result of kinase activity of SiaB.

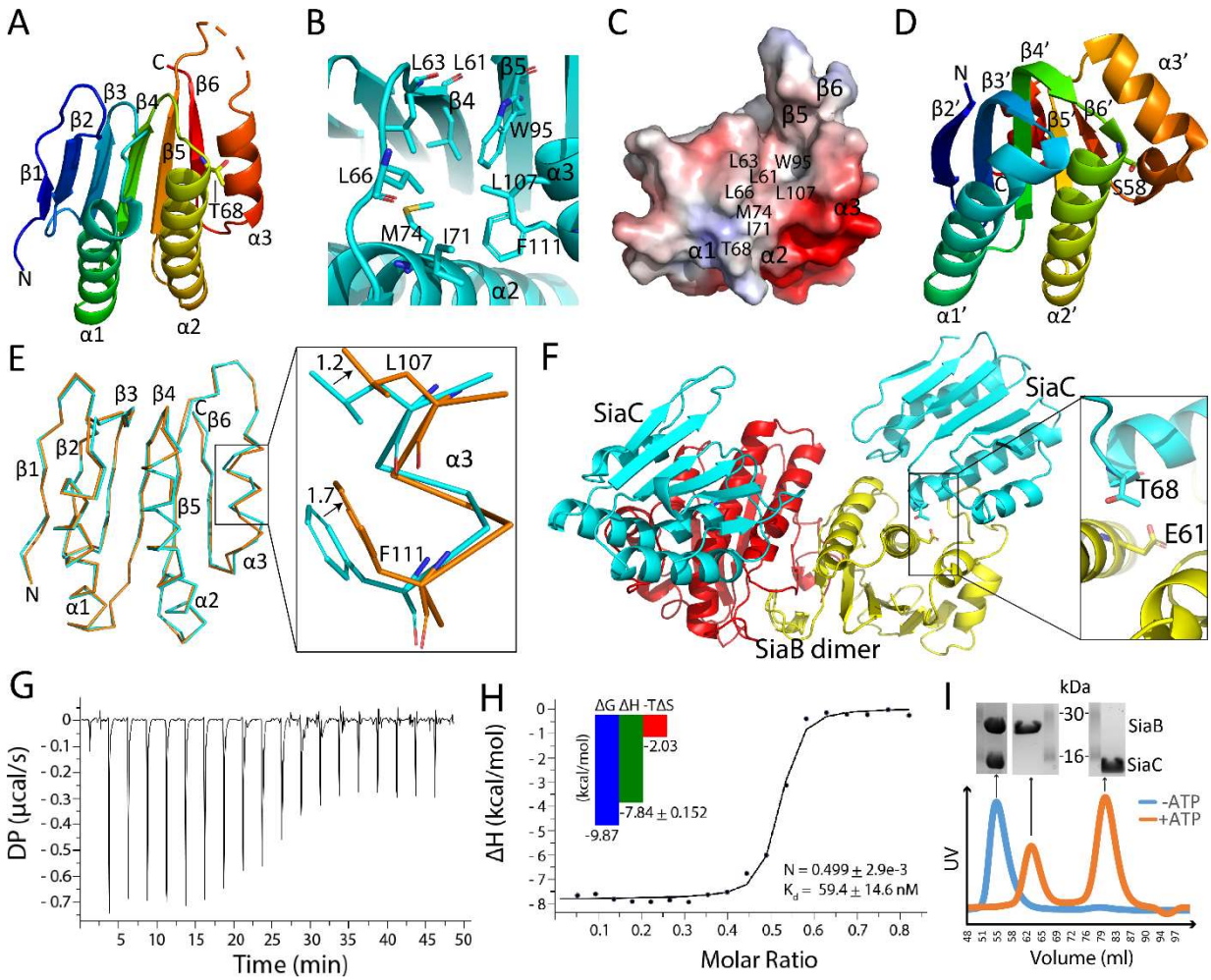

Figure 7: (A) "Rainbow" representation of SiaC. The phosphorylation site T68 is shown as sticks. **(B)** Hydrophobic pocket of SiaC next to T68. **(C)** Surface electrostatic potential of SiaC with the hydrophobic pocket labelled**.** The structure is displayed in the same orientation as in panel B**. (D)** "Rainbow" representation of SpollAA (PDB code: 4QTP). The phosphorylation site S58 is shown as sticks. **(E)** Alignment of energy-minimized SiaC with energy-minimized $SiaC^P$ with RMSD of 0.5 Å. The $SiaC^P$ structure was derived from SiaC by substitution of T68 with pT68 (see Supplementary for detailed information). L107 and F111 are further away from the hydrophobic pocket in $SiaC^P$ than they are in SiaC. **(F)** Model of SiaB/SiaC complex generated by superimposition of the SiaB model (*red* and *yellow*) and SiaC (*cyan*) to SpollAA/SpollAB complex (PDB code: 1THN) and subsequent manual adjustment and energy minimization to eliminate clashes. E61 of SiaB and T68 of SiaC are shown as sticks. **(G and H)** Isothermal titration calorimetry result after injecting 270 µM SiaC to a solution containing 64 µM SiaB. Heat release of binding was measured by differential power (DP). A strong binding was observed with a K_d of 59.4 nM. **(H)** Size exclusion chromatography profiles derived by UV-Absorption for SiaB/SiaC mixtures (1:1 molar ratio) in the presence (*orange line*) or absence (*blue line*) of 10 mM ATP and 20 mM $MgCl_2$. The SDS-PAGE analysis of the proteins causing the peaks in the size exclusion chromatography are shown above the profiles.

310 ***Molecular Docking and MD simulation of SiaC^P with the phosphatase domain of SiaA***

311 As SiaA-PP2C targets SiaC^P, a transient binding of these two proteins is likely to occur. To study the
312 interaction between SiaA and SiaC during the dephosphorylation reaction, we performed a MD simulation
313 on SiaA binding to SiaC and SiaC^P. The SiaA-SiaC complex was predicted by molecular docking of SiaA-PP2C
314 dimer and SiaC^P-SiaC using ZDOCK, followed by 60 ns of MD simulation (**Figure 8A and B**). These
315 experiments demonstrated that the phosphorylated pT68 is required for productive binding to the
316 catalytic site of SiaA-PP2C, where it remains efficiently bound via the catalytic Mg^{2+} ion M3 and the
317 bridging water molecules surrounding it (**Figure 8C-E**). This result is consistent with the experimental
318 observation that only pT68 in SiaC^P constitutes the substrate for SiaA-PP2C activity. In contrast, the non-
319 phosphorylated T68 dissociated from the catalytic site in less than 15 ns of simulation, suggesting that
320 SiaC will quickly dissociate from SiaA upon dephosphorylation.

321 Based on the simulated model, several key interactions that could contribute to substrate specificity of
322 SiaA-PP2C were identified. First, R652 stabilizes the positively charged phosphate group of pT68 through
323 the formation of a salt bridge (**Figure 8F**). In addition, the flexible loop between α5 and α6 of SiaA inserts
324 in a shallow pocket located between α2, α3, β4, β5 and β6 of SiaC^P and establishes hydrophobic contacts
325 with L61, L66, I71, M74, M75, L78, W95, L107 and F111 through F612 (**Figure 8G**). Notably, the salt bridge
326 identified between R618 and E609 of SiaA is likely to restrain the orientation of the flexible loop between
327 α5 and α6, which could favours interaction with SiaC^P. The non-aggregative mutant Δ*siaA* was recently
328 found to harbor deletion of two amino acids in the phosphatase domain of SiaA (G611F612; SiaA-PP2C*)[70].
329 To gain a deeper insight into the underlying mechanism for the loss of function in SiaA-PP2C*, we
330 generated a homology model using SWISS-MODEL (https://swissmodel.expasy.org/) with the SiaA-PP2C
331 crystal structure as template (GMQE =0.98, QMEAN = -0.54). Notably, the deleted amino acids G611F612
332 map to the flexible loop between α5 and α6, and F612 is the essential residue for interaction with the
333 hydrophobic pocket of SiaC^P **(Figure 8H1-I2)**. Thus, it is possible that by being unable to form this

hydrophobic contact, SiaA-PP2C* cannot accommodate its substrate and is therefore unable to dephosphorylate SiaC^P.

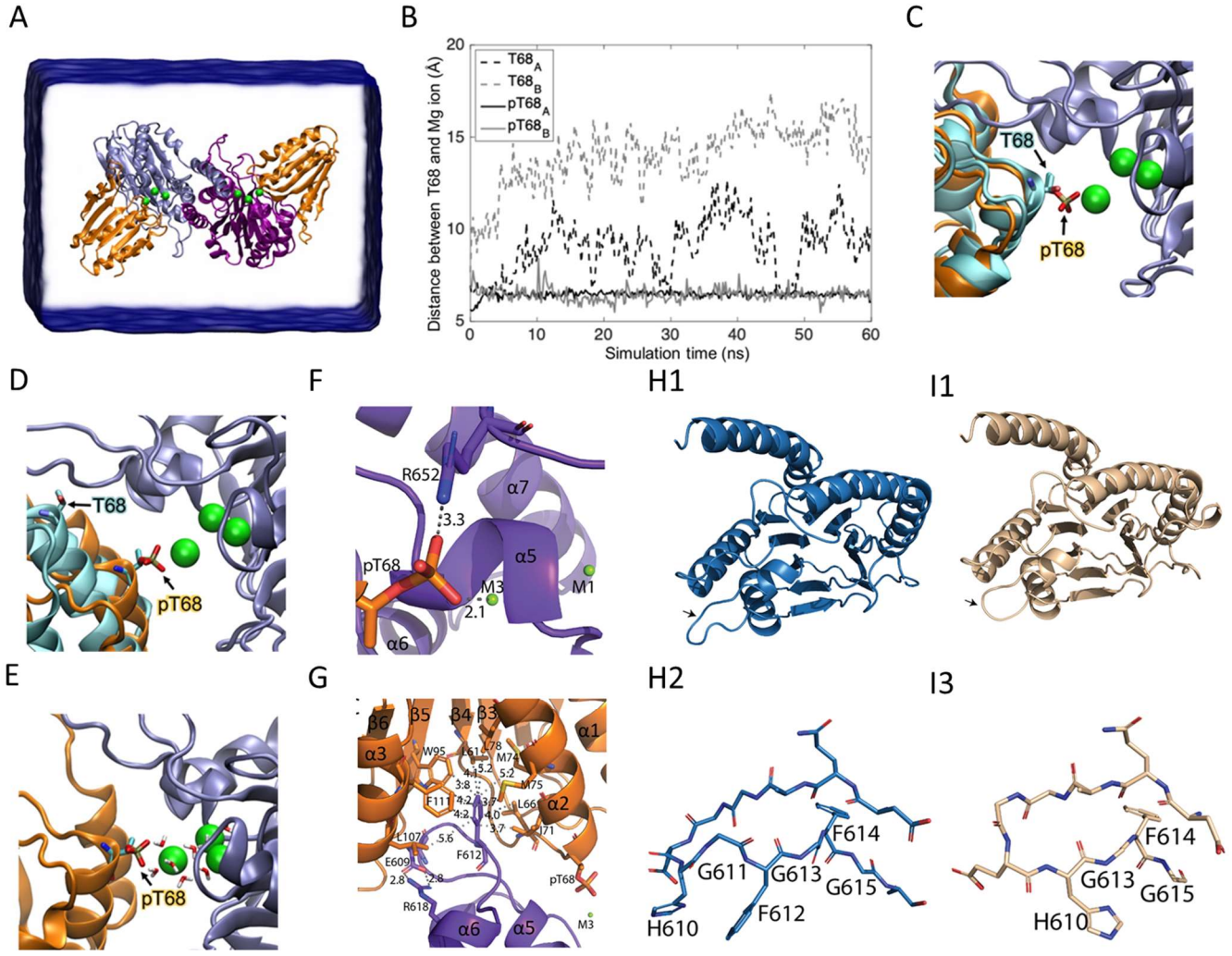

Figure 8: Binding of SiaA-PP2C to phosphorylated SiaC. **(A)** The simulated system using ZDOCK contains a SiaA-PP2C dimer (*blue/purple ribbon*) with SiaC (*cyan ribbon*) or SiaC^P (*orange ribbon*) docked to each SiaA-PP2C monomer. **(B)** Distance between Cα of T68/pT68 and Mg^{2+} ion (M3). Phosphorylated T68 of both SiaC^P (*black and grey solid lines*) remains coordinated with the Mg^{2+} ion (*green sphere*). Unphosphorylated T68 (*black and grey dashed lines*) dissociates from the Mg^{2+} ion in less than 15 ns. The positions of T68 and Mg^{2+} ions before **(C)** and after the simulation **(D)** are displayed in the same color code as in panel A. **(E)** The pT68 of SiaC^P is interacting with the bridging water molecules for the entire 60 ns of simulation. **(F-G)** Cartoon representations of specific parts of the SiaA-PP2C/SiaC^P complex after 60 ns of simulation. SiaC^P is coloured in orange; SiaA-PP2C dimer is coloured in purple and blue **(F)** Interaction of pT68 with R652 and M3. R652 might be important for stabilisation of the complex through the formation of a salt bridge. pT68 remains in close proximity with M3 (2.1 Å). **(G)** F612 interacts with the hydrophobic pocket of SiaC^P. Salt bridge formation between R618 and E609 in SiaA-PP2C might restrain the orientation of the flexible loop between α5 and α6 to accommodate its interaction with the hydrophobic pocket of SiaC^P. Cartoon representation of SiaA-PP2C **(H1)** and a homology model of the mutant allele SiaA-PP2C* **(I1)** from the Δ*siaA* mutant, in which G611 and F612 at the flexible loop between α5 and α6 are deleted (*black arrows*). Stick representation of the flexible loop of SiaA-PP2C **(H2)** and SiaA-PP2C* **(I2)**.

338 **Discussion**

339 The need to develop novel strategies to control bacterial infections is well documented and is driven by
340 the steadily increasing threat of antimicrobial resistance and the lack of new antibiotic targets, which has
341 become one of the biggest challenges for public health systems with immense financial burdens[82,83].
342 Attached or suspended biofilms contribute to the severity of this problem as they are often observed
343 during infections, are responsible for increased phenotypic heterogeneity due to the establishment of
344 chemical microenvironments, display inherent tolerance to biocides and are better protected against the
345 host immune system including phagocytes or neutrophils[16,25–28,62,65–68,84]. It has been demonstrated that
346 disruption of the biofilm life-cycle can either lead to natural clearance of the biofilm from the host by the
347 immune function, or that biofilm inhibitors can be combined with antimicrobials for better killing of the
348 pathogen[39,85,86]. As such, biofilm-related signal interference has significant, yet mostly unrealized,
349 potential to be exploited as a novel anti-infective strategy[87–90].

350 The SiaA and/or SiaD proteins are essential for the formation of macroscopic aggregates during growth in
351 the presence of the toxic surfactant SDS or the ROS-generating biocide tellurite in a c-di-GMP
352 manner[12,70,72]. This active and energy requiring response may represent an adaptive survival strategy as
353 the corresponding aggregates were found to protect cells of the same, as well as other, species in mono-
354 and mixed culture experiments[16,71,91]. The present study expands the roles of SiaA and SiaD and reveals
355 their importance in cellular aggregation in response to carbon availability and further demonstrate that
356 the protein kinase SiaB and the anti-sigma factor antagonist-like SiaC protein, which are both part of the
357 *siaABCD* operon[70], are also involved this regulation.

358 The connection of the metabolic/energy status of a cell and the SiaABCD-dependent cellular aggregation
359 is intriguing, as the lungs of CF patients, which are prone to chronic infection by *P. aeruginosa*, are
360 characterized by the presence of increased concentrations of different carbon sources that *P. aeruginosa*
361 can utilise for growth. These carbon sources include, but are not limited to, glucose[92], short-chain fatty

362 acids[93,94], ethanol and 2,3 butanediol[95–97]. This is particularly important because ethanol and 2,3-
363 butanediol have recently been reported to influence microbial colonisation of epithelial cells or the
364 persistence of microbes during infection[18,98,99]. It is thus possible that the SiaABCD signalling pathway is
365 not only involved in the regulation of cellular aggregation but also has an impact on virulence traits of *P.*
366 *aeruginosa*. This hypothesis is supported by several observations:

367 *i)* A diverse set of regulatory systems involved in biofilm formation and/or virulence are interconnected
368 with the SiaABCD pathway. These include the transcriptional regulators AmrZ and FleQ or the
369 posttranscriptional regulatory systems RsmA/*rsmY*/*rsmZ*, RsmN and CRC[72,100–104].

370 *ii)* SiaD modulates the community structure and competitiveness of *P. aeruginosa* cells within dual-
371 species biofilms with cells of *Staphylococcus aureus* and impacts pyoverdine and pyocyanine
372 production[12,71,105].

373 *iii)* SiaD was identified as one of the DGCs capable of initiating the "Touch-Seed-and-Go" virulence
374 program by activating the c-di-GMP receptor FimW[106]. This activation leads to the attachment of cells
375 and the subsequent induction of virulence traits through asymmetric cell division, finally promoting
376 efficient tissue colonization, localised host damage and fast dissemination of the infection.

377 Overall, this highlights that the SiaABCD pathway represents an attractive target for signal interference
378 for therapeutic interventions. However, for the development of any signal interference drug, an in-depth
379 knowledge about the underlying molecular mechanisms of the target pathways is a prerequisite. Here,
380 we provide compelling evidence that the SiaABC proteins make use of a partner switch mechanism to
381 balance cellular aggregation in response to carbon availability and propose that SiaD activity is the final
382 target of this regulation. A partner switch system (PSS) typically involves a PP2C phosphatase (SiaA), an
383 anti-sigma factor with kinase activity (SiaB) and anti-sigma factor antagonist representing the target for
384 phosphorylation (SiaC). In line with such a mechanism, the phosphorylation status of the proposed anti-
385 sigma factor antagonist SiaC is crucial for the switch to occur. While SiaC showed a strong binding to SiaB,

386 the binding affinity was significantly reduced after phosphorylation. Based on our bioinformatics
387 approach, the dissociation upon SiaB activity shares a similar mechanism of action to that of SpoIIAA and
388 SpoIIAB, where phosphorylation of the anti-sigma factor antagonist SpoIIAA only results in small structural
389 changes but leads to a rapid dissociation from the anti-sigma factor SpoIIAB due to electrostatic and steric
390 clashes[79]. Although SiaABC resembles the SpoIIAA-AB-sigma^F and SpoIIE system, we propose that its role
391 is likely not the sequestration of a sigma factor, but rather to regulate c-di-GMP biosynthesis of SiaD. Our
392 proposal is based on recent studies that described partner switches that indeed regulate DGC activity. In
393 *P. aeruginosa*, the HptB-HsbR-HsbA system was shown to promote DGC activity of HsbD following its
394 interaction with the phosphorylatable anti-sigma factor antagonist HsbA, finally regulating biofilm
395 formation and swimming motility[107]. More recently, a PSS was shown to be involved in mixed-linkage ß-
396 glucan synthesis in *S. meliloti* through the induction of c-di-GMP levels[108]. In this system, the Ser/Thr-
397 specific phosphatase/kinase couple BgrU/BgrW controls the phosphorylation status of the BgrV protein
398 and hence controls the activity of the DGC BgrR.

399 We were unable to purify the SiaD protein in a soluble form to directly test the proposed interaction of
400 SiaD with SiaC and/or SiaC^P. However, based on the similarities described above, we propose a model in
401 which both SiaA and SiaB balance the phosphorylation status of SiaC at position T68 that in turn directly
402 influences the activity of SiaD. In this scenario, the activation of SiaA shifts the equilibrium of SiaC/SiaC^P
403 towards the phosphorylated form through SiaB activity. This would stimulate biosynthesis of c-di-GMP by
404 SiaD resulting in increased cellular aggregation, most likely through influencing the direct interaction of
405 SiaD with either SiaC and/or SiaC^P. As a negative feedback response, SiaC^P has an increased binding affinity
406 towards SiaA, which downregulates SiaD activity through the dephosphorylating of T68 and thereby
407 inversely affecting protein interactions.

408 We identified the PP2C domain of SiaA and the putative anti-sigma factor antagonist SiaC as prime targets
409 for the development of biofilm interference drugs. The PP2C-type phosphatase SiaA, while conserved in

410 prokaryotes and eukaryotes, is structurally unique. A Flap sub-domain, suggested of being involved in
411 substrate interaction and specificity, has been reported in human PPM1A and many other PP2C-type
412 phosphatases[78]. SiaA-PP2C lacks the Flap sub-domain and instead has a long loop between β7 and β8 that
413 does not seem to interact with $SiaC^P$ according to MD simulations. However, the flexible loop between α5
414 and α6 might aid in substrate specificity of SiaA by interacting with the hydrophobic pocket of SiaC near
415 the phosphorylation site. Although further studies are needed to confirm this finding, the fact that the
416 phosphatase domain of the mutant allele SiaA-PP2C* has a deletion in G611F612, of which the latter
417 residue seems to be crucial for the interaction with SiaC, is supportive of this hypothesis. Thus, the design
418 of drugs targeting the flexible loop in SiaA, could be exploited to interfere with SiaA/$SiaC^P$ interaction and
419 hence, block downstream induction of biofilm formation through the inhibition of $SiaC^P$
420 dephosphorylation. SiaC also represents an exciting target for interference, as it is structurally most
421 similar to bacterial anti-sigma factor antagonists with little homology with human proteins. The
422 hydrophobic pocket next to the phosphorylation site of SiaC is of particular interest, as it seems to be
423 involved in the stability of the SiaA/SiaC interaction. In addition, a large patch of negatively charged
424 surface is present at α2 and α3 near the hydrophobic pocket **(Figure 7C)**, and could thus be useful for drug
425 design as potential anchor points.

426 The high-resolution structures for of these target proteins will allow the *de novo* design of small molecule
427 drugs or synthetic peptides. Using physiological mid-throughput assays based on biofilm formation, novel
428 drugs can also be screened for their ability to penetrate cells, which is of essential importance to reach
429 the proposed interference target sites. In this regard, it is interesting to note that the use of engineered
430 phages as delivery vehicles for protein and/or peptide-based drugs represents a suitable and highly
431 attractive approach to potentially overcome this obstacle[109–113]. As an alternative to the *de novo* design
432 approach, existing drug and small molecule libraries as well as synthetic peptide libraries could be
433 screened for activity against these targets.

434 In summary, the presented work provides a deeper understanding of the SiaABCD mediated regulation
435 by expanding the fundamental genetic and biochemical mechanisms that control cellular aggregation in
436 response to carbon availability and it potentially paves the way for the development of novel biofilm-
437 interference drugs and combinatorial therapies, which are desperately needed to combat the rising
438 antibiotics crisis.

439

440 ## Materials and methods

441 ***Strains and growth conditions***

442 Bacterial strains (**Table S1**) were maintained on Lysogeny Broth (LB) (Bertani 1951) solid medium (1.5%
443 agar w/v) and routinely cultured in 10 mL LB medium in 50 mL Falcon tubes (Greiner Bio-one) or M9
444 medium (47.6 mM Na_2HPO_4, 22 mM KH_2PO_4, 8.6 mM NaCl, 18.6 mM NH_4Cl, 2 mM $MgSO_4$, 0.1 mM $CaCl_2$,
445 0.03 mM $FeCl_2$) with shaking at 200 rpm and incubation at 37°C or 30°C. Where indicated, antibiotics were
446 added.

447 ***Scanning electron microscopy (SEM)***

448 For SEM, overnight cultures of *P. aeruginosa* strains were prepared in 10 mL LB in 50 mL Falcon tubes and
449 incubated for 16 h at 30°C with shaking at 200 rpm. Following incubation, cultures were harvested by
450 centrifugation for 2 min at 16,060 × *g* at room temperature and washed twice in 1 mL of fresh M9 minimal
451 medium. These cells were used to inoculate 50 mL of medium supplemented with 22.2 mM glucose with
452 an OD_{600} = 0.05 in a 250 mL Erlenmeyer flask and incubated for 5.5 h at 30°C with shaking at 200 rpm.
453 Experiments were performed as three independent replicates, which were subsequently pooled together.
454 Pooled samples were pipetted onto poly-L-lysine coated coverslips on the bottom of the wells of a 12 well
455 plate, using enough culture to create a convex droplet without flooding past the edges of the coverslip. A
456 detailed description of the method of SEM sample preparation is provided in the supplementary material
457 file. Finally, samples were sputter coated with gold for 2.5 min at 40 mA (Emitech, K550X). Conductive
458 samples were then analysed by SEM using a spot size of 3, voltage at 15 kV and a working distance of 10
459 mm (FEI Quanta 200 ESEM). Multiple fields of view were imaged randomly for each sample and
460 representative images are shown.

461 ***Phenotypic characterisation in 12 well plates***

462 For phenotypic characterisation of cultures during growth on 3.5 mM SDS and 22.2 mM glucose, cell
463 culture treated, 12 well microtiter plates with 2 mL M9 medium were prepared and inoculated with

464 washed cells from an overnight culture grown in LB medium to an OD_{600} = 0.01. Following incubation at
465 30°C with shaking at 200 rpm for 18 h the plates were imaged at 1200 dpi using an Umax Powerlook 1000
466 flatbed scanner with V4.71 software in a dark room. Images were normalised using Adobe Photoshop CS5
467 Software by using the 'match colour' image adjustment function, with all images normalised to the first
468 image scanned using this experimental format. Experiments were performed as at least 6 independent
469 replicates and representative images are shown.

470 ***Biofilm quantification using crystal violet staining in 24 well plates***

471 A microtitre based crystal violet (CV) staining assay was used to quantify biofilm formation during growth
472 with various media. Cell culture treated and non-treated 24 well microtiter plates with 800 µL M9 medium
473 were prepared and inoculated with washed cells from an overnight culture grown in LB medium to an
474 OD_{600} = 0.01. M9 medium was supplemented with 22.2 mM glucose, 20 mM succinate, 40 mM ethanol or
475 20 mM 2,3-butanediol and incubated at 30°C with shaking at 200 rpm. Following incubation, liquid
476 cultures were removed, pooled and used for quantification of the carbon source and optical density
477 measurements. The wells of the microtitre plates were then stained with 900 µL CV solution (0.1% [w/v]
478 stock in water) for 10 min without shaking. After incubation, the liquid was discarded and the wells of the
479 microtitre plates were washed with 1 mL Tris-HCl (10 mM; pH 7) containing 0.9 % NaCl (w/v) for 10 min,
480 once without and once with shaking at 200 rpm. Subsequently, the plates were air dried and the remaining
481 CV was solubilised by incubation with 1 mL of pure ethanol for 10 min with shaking at 200 rpm.
482 Quantification of CV was quantified at 595 nm in a microtiter plate reader.

483 ***Particle size experiments***

484 Strains were inoculated in 20 mL LB medium (244620, BD Difco) in a 100 mL Erlenmeyer flask and
485 incubated at 30°C with 200 rpm shaking. Overnight cultures were subsequently aliquoted to 50 mL falcon
486 tubes and centrifuged at 9500 × *g* for 5 min. The supernatant was discarded and the pellet was
487 resuspended in 10 mL of M9 medium containing 22 mM glucose. The washing step was repeated once

488 with the pellet resuspended in 2 - 5 mL of M9 medium. Finally, the cell suspensions were passed five times
489 through a 25 gauge syringe needle to disrupt cell aggregates. The optical density of the suspension was
490 adjusted to OD_{600} = 2 and 1 mL was added to 20 mL of M9 medium supplemented with glucose in an 100
491 mL Erlenmeyer flask at a final OD_{600} = 0.1. The cultures were subsequently incubated at 30°C with shaking
492 at 200 rpm. Samples were collected at 3 and 6 h for OD_{600} measurement and quantification of glucose
493 concentration. After 6 h of incubation, when glucose was not yet exhausted from the medium, the
494 cultures were analysed with a particle size analyser (SALD 3101, Shimadzu) using a pump speed of 4.0,
495 and the accompanying software was used for analysis of the data (WingSALDII version 3.0.0). Particle sizes
496 of between 0.5 – 3000 µM were selected for analysis. Calculations were based on water as the dispersing
497 agent with a refractive index of 1.70-020i. Data are presented as the cumulative percentage of the
498 biovolume of the particles within a given size range (0.5 – 10 uM, 10 – 200 uM, 200 – 3000 uM) compared
499 to all particle in the sample. Two biological replicates were analysed and from each sample, the particle
500 size distribution was quantified with three subsequent measurements. Data are presented as the mean
501 value of technical triplicates from a single experiment with the error representing the technical variation.

502 ***Enzymatic assays***

503 For enzymatic activity measurements the purified SiaA-PP2C protein fragment of *P. aeruginosa* PAO1 was
504 used. The phosphatase activity of SiaA-PP2C was accessed using either para-nitrophenyl phosphate
505 (pNPP) or the purified $SiaC^P$ protein as the target substrate. For assays with pNPP as the substrate,
506 phosphatase activity was determined via the production of a colorimetric p-nitrophenolate product that
507 absorbs strongly at 405 nm. Four times working solutions of the protein (4×: 200 µg/mL; 1×: 50 µg/mL
508 [~1.49 µM]) were made in water and mixed with equal volume of pNPP phosphatase assay buffer (1×: 20
509 mM Tris-HCl [pH 7.5], 150 mM NaCl, 0 – 20 mM $MnCl_2$). For Michaelis-Menten kinetics studies, a higher
510 concentration of 100 mM Tris-HCl [pH 7.5] buffer was used to provide a higher buffering capacity at high
511 pNPP concentrations. Fifty µL of the mixture was then added to each well in 96 well plates, following

512 which pNPP was added to a final concentration of 0 – 20 mM to make up a final volume of 100 μL per
513 well. Phosphatase activity over time was detected via the measurement of the absorbance at 405 nm
514 using a microtitre plate reader at 37°C (Tecan Infinite M200 Pro). To calculate concentrations, p-
515 nitrophenol (Sigma, #1048) was dissolved in phosphatase assay buffer and 100 uL of 0 – 390 μM samples
516 were used to generate a calibration curve of p-nitrophenolate concentrations against absorbance in a 96-
517 well plate. Enzyme kinetics were determined using the initial rates of reaction of p-nitrophenolate
518 formation from 0 – 10 min (μM min^{-1}) against pNPP substrate concentration and curve fitting with
519 Graphpad Prism V8.00 using the parameter [Et] = 1.49 μM. Specific activities (kU mg^{-1}) were obtained by
520 division with 0.005 mg of SiaA used per reaction well.

521 ***Malachite green phosphate assays and ADP-Glo™ assays***

522 Phosphatase and kinase activities of SiaA and/or SiaB on SiaC and/or $SiaC^p$ were determined using the
523 Malachite green phosphate assay kit (Sigma Aldrich) and ADP-Glo™ assay kit (Promega) respectively. 0.5
524 μM of SiaA and/or SiaB was incubated with 0 – 5 μM of SiaC or $SiaC^p$ in the reaction buffer (20 mM Tris-
525 HCL [pH 7.5], 150 mM NaCl with addition of 0 – 25 mM ATP and 0 – 20 mM $MnCl_2$ and/or 0 – 20 mM
526 $MgCl_2$) for 1 h at 37°C. Subsequently, the reactions were stopped and the amount of phosphate released
527 in phosphatase reactions or ATP consumed in kinase reactions was determined in accordance to the
528 commercial kit protocols. Briefly, for Malachite green assays, 20 μL of the kit working solution was added
529 to 80 μL of the sample to stop the reaction. The mixture was then incubated at room temperature for 30
530 min for the generation of a green complex formed between Malachite Green, molybdate and free
531 orthophosphate. Measurements were taken at 620 nm using a microplate reader. Readings were then
532 converted to phosphate measurements using a standard curve. For ADP-Glo™ assays, 20 uL of the ADP-
533 Glo™ reagent was added to 20 uL of the sample to stop the reaction and deplete remaining ATP. If enzyme
534 reactions were carried out in the absence of Mg^{2+}, $MgCl_2$ was supplemented to the mixture to a final
535 concentration of 20 mM. The mixture was incubated at room temperature for 40 min. A second kinase

536 detection reagent was added to the mixture to convert ADP consumed to ATP and for conversion of the
537 ATP signal to luminescence signals and further incubated for 45 min. Luminescence was measured using
538 a microplate reader and converted to ATP consumed in kinase reaction using a standard curve generated.
539 At least two independent replicates with technical duplicates were carried out for each enzymatic
540 reaction.

541 ***MS fingerprinting analysis of SiaC phosphorylation state***

542 For assays with $SiaC^P$ as substrate, phosphatase activity was determined using the protein that was initially
543 produced and purified from strain Δ*siaA* (see supplementary material file for detailed information). To
544 elucidate the phosphorylation site in the SiaC protein, 20 µg of purified $SiaC^P$ was incubated in the absence
545 or presence of 20 µg of purified SiaA for 1 h at 37°C in a final volume of 40 µL assay solution (20 mM HEPES
546 [pH 7.5], 300 mM NaCl, 0.02 % β-mercaptoethanol, 0.1 mg mL^{-1} BSA, 5 % glycerol, 5 mM Mn^{2+}, 1 mM
547 EDTA). After 2 h of incubation at 30°C, 20 µL were used for the separation of the two proteins using a 15
548 % SDS-PAGE gel. The SiaC protein band (17 kDa) was excised from the SDS-PAGE gel, and the gel sample
549 was submitted to shotgun peptide mass spectrometry (PMS) analysis, to identify SiaC and its
550 phosphorylation state at threonine residue 68 (T68)[73]. Therefore, the relative abundance of signals in the
551 PF-MS fragmentation-mass spectra for the specific peptide containing the phosphorylation site T68 (i.e.,
552 peptide LLYLN**T**SSIK) in a non-phosphorylated state (parental fragmentation-mass spectrum for peptide
553 LLYLN**T**SSIK) and for mass-shifts indicating its phosphorylation (peptide LLYLN**T**SSIK with monoisotopic
554 mass-change, +79.96633 Da; average mass-change +79.9799 Da), was determined (see Supplementary
555 for more details).

556 ***Analytics of supernatants***

557 For glucose quantification, the liquid cultures were filtered through a 0.22 µM PES filter (PN 4612, Pall)
558 and quantified using the GO assay kit (GAGO20, Sigma Aldrich). Briefly, one volume of sample or standard
559 solution (20 µL) was mixed with two volumes of assay reagent (40 µL) in a 96 well plate and incubated

560 statically at 37°C for 30 min. Subsequently, the reaction was stopped by the addition of 12 N H_2SO_4 (40
561 µL) to the reaction mixture. Glucose concentrations were quantified at 540 nm using a microplate reader
562 (Infinite 200 pro, Tecan). Zero – 80 µg mL^{-1} glucose standard solutions were used for the calibration curve.

563 Concentrations of succinate, ethanol and 2,3-butanediol were quantified by a HPLC method using an
564 Aminex HPX-87H 300 x 7.8 mm ion-exchange column (BioRad, Munich, Germany) heated to 60°C. The
565 eluent was 5 mM H_2SO_4, which was delivered to the column by a LC-10ATvp pump (Shimadzu, Munich,
566 Germany) at a flow rate of 0.6 mL min^{-1}. The eluent was continuously degassed with a DGU-20A3R
567 degassing unit (Shimadzu, Munich, Germany). Samples were injected using 10 µL with a 234 autosampler
568 (Gilson, Limburg-Offheim, Germany). Resolved compounds were analysed with a refractive index detector
569 (RID-10A, Shimadzu, Munich, Germany) and the data processed using the Shimadzu Lab solutions
570 software version 5.81. Concentrations were finally calculated from calibration curves of the corresponding
571 metabolite of interest.

572 ***Statistical analysis***

573 Data ($n \geq 3$) were analysed using a two-sided students *t*-tests ($\alpha = 0.05$) with *p*-values < 0.05 interpreted
574 as being significantly different.

575 ***Additional methods and procedures***

576 Detailed methods for construction of the *siaB* and *siaC* mutant strains, the construction of plasmids, and
577 the production and purification, crystallization and/or shotgun peptide mass spectrometry, as well as the
578 procedure for the generation of homology models, molecular docking experiments, and procedures for
579 MD simulations are described within the supplementary material file.

580 **Funding**

581 The work of Janosch Klebensberger, Wee Han Poh, Julien Lescar, Jianqing Lin, Scott A. Rice was partially
582 supported by a joint mobility grant funded by the Federal Ministry of Education and Research in Germany

583 (FKZ: 01DP17004) and the Ministry of Trade and Industry in Singapore (SGP-PROG3-023. 2017). We
584 acknowledge financial support from the Singapore Centre for Environmental Life Sciences Engineering,
585 whose research is supported by the National Research Foundation Singapore, Ministry of Education,
586 Nanyang Technological University and National University of Singapore, under its Research Centre of
587 Excellence Programme as well as funding from the Ministry of Education (tier 1, grant RG154/14).

588 Acknowledgements

589 The authors further declare that the research was conducted in the absence of any commercial or financial
590 relationships that could be construed as a potential conflict of interest. Janosch Klebensberger would like
591 to thank Prof. Bernhard Hauer for his continuous support. We also acknowledge beam time allocation at
592 the SOLEIL synchrotron. The MD simulations for this article were performed on ASPIRE 1 of the National
593 Supercomputing Centre, Singapore (https://www.nscc.sg).

594 References

595 1. Stoodley, P., Sauer, K., Davies, D. G. & Costerton, J. W. Biofilms as complex differentiated
596 communities. *Annu. Rev. Microbiol.* **56,** 187–209 (2002).
597 2. Flemming, H. C. *et al.* Biofilms: an emergent form of bacterial life. *Nat. Rev. Microbiol.* **14,** 563–575
598 (2016).
599 3. Costerton, J. W., Lewandowski, Z., Caldwell, D. E., Korber, D. R. & Lappin-Scott, H. M. Microbial
600 biofilms. *Annu. Rev. Microbiol.* **49,** 711–745 (1995).
601 4. Flemming, H. C. & Wuertz, S. Bacteria and archaea on Earth and their abundance in biofilms. *Nat.*
602 *Rev. Microbiol.* **17,** 247–260 (2019).
603 5. Flemming, H.-C. & Wingender, J. The biofilm matrix. *Nat. Rev. Microbiol.* **8,** 623–633 (2010).
604 6. McDougald, D., Rice, S. A., Barraud, N., Steinberg, P. D. & Kjelleberg, S. Should we stay or should
605 we go: mechanisms and ecological consequences for biofilm dispersal. *Nat. Rev. Microbiol.* **10,** 39–
606 50 (2012).
607 7. Ciofu, O., Tolker-Nielsen, T., Jensen, P. O., Wang, H. & Hoiby, N. Antimicrobial resistance,
608 respiratory tract infections and role of biofilms in lung infections in cystic fibrosis patients. *Adv.*
609 *Drug. Deliv. Rev.* **85,** 7–23 (2015).
610 8. Davey, M. E. & O'Toole G, A. Microbial biofilms: from ecology to molecular genetics. *Microbiol. Mol.*
611 *Biol. Rev.* **64,** 847–867 (2000).
612 9. Gilbert, P., Maira-Litran, T., McBain, A. J., Rickard, A. H. & Whyte, F. W. The physiology and collective

613 recalcitrance of microbial biofilm communities. *Adv. Microb. Physiol.* **46,** 203–256 (2002).

614 10. Hoiby, N., Bjarnsholt, T., Givskov, M., Molin, S. & Ciofu, O. Antibiotic resistance of bacterial biofilms.
615 *Int. J. Antimicrob. Agents* **35,** 322–332 (2010).

616 11. Mah, T.-F. *et al.* A genetic basis for *Pseudomonas aeruginosa* biofilm antibiotic resistance. *Nature*
617 **426,** 306–310 (2003).

618 12. Chua, S. L. *et al.* C-di-GMP regulates *Pseudomonas aeruginosa* stress response to tellurite during
619 both planktonic and biofilm modes of growth. *Sci. Rep.* **5,** 10052 (2015).

620 13. Barraud, N. *et al.* Involvement of nitric oxide in biofilm dispersal of *Pseudomonas aeruginosa*. *J.*
621 *Bacteriol.* **188,** 7344–7353 (2006).

622 14. Hoffman, L. R. *et al.* Aminoglycoside antibiotics induce bacterial biofilm formation. *Nature* **436,**
623 1171–1175 (2005).

624 15. Gotoh, H. *et al. Pseudomonas aeruginosa*, under DNA replication inhibition, tends to form biofilms
625 via Arr. *Res. Microbiol.* **159,** 294–302 (2008).

626 16. Klebensberger, J., Rui, O., Fritz, E., Schink, B. & Philipp, B. Cell aggregation of *Pseudomonas*
627 *aeruginosa* strain PAO1 as an energy-dependent stress response during growth with sodium
628 dodecyl sulfate. *Arch. Microbiol.* **185,** 417–427 (2006).

629 17. Schleheck, D., Dong, W., Denger, K., Heinzle, E. & Cook, A. M. An α-proteobacterium converts linear
630 alkylbenzenesulfonate surfactants into sulfophenylcarboxylates and linear
631 alkyldiphenyletherdisulfonate surfactants into sulfodiphenylethercarboxylates. *Appl. Environ.*
632 *Microbiol.* **66,** 1911–1916 (2000).

633 18. Chen, A. I. *et al.* Candida albicans Ethanol Stimulates *Pseudomonas aeruginosa* WspR-Controlled
634 Biofilm Formation as Part of a Cyclic Relationship Involving Phenazines. *PLoS Pathog.* **10,** e1004480
635 (2014).

636 19. Létoffé, S., Audrain, B., Bernier, S. P., Delepierre, M. & Ghigo, J.-M. Aerial Exposure to the Bacterial
637 Volatile Compound Trimethylamine Modifies Antibiotic Resistance of Physically Separated Bacteria
638 by Raising Culture Medium pH. *MBio* **5,** :e00944–13 (2014).

639 20. Baghal Asghari, F., Nikaeen, M. & Mirhendi, H. Rapid monitoring of *Pseudomonas aeruginosa* in
640 hospital water systems: a key priority in prevention of nosocomial infection. *FEMS Microbiol Lett*
641 **343,** 77–81 (2013).

642 21. Kerr, K. G. & Snelling, A. M. *Pseudomonas aeruginosa*: a formidable and ever-present adversary. *J.*
643 *Hosp. Infect.* **73,** 338–344 (2009).

644 22. Williams, M. M., Armbruster, C. R. & Arduino, M. J. Plumbing of hospital premises is a reservoir for
645 opportunistically pathogenic microorganisms: a review. *Biofouling* **29,** 147–162 (2013).

646 23. Pawar, V. *et al.* In vivo efficacy of antimicrobials against biofilm-producing *Pseudomonas*
647 *aeruginosa*. *Antimicrob. Agents Chemother.* **59,** 4974–4981 (2015).

648 24. Malone, J. G. *et al.* YfiBNR mediates cyclic di-GMP dependent small colony variant formation and
649 persistence in *Pseudomonas aeruginosa*. *PLoS Pathog.* **6,** e1000804 (2010).

650 25. Pestrak, M. J. *et al. Pseudomonas aeruginosa* rugose small-colony variants evade host clearance,
651 are hyper-inflammatory, and persist in multiple host environments. *PLoS Pathog.* **14,** e1006842
652 (2018).

653 26. Bjarnsholt, T. *et al. Pseudomonas aeruginosa* biofilms in the respiratory tract of cystic fibrosis
654 patients. *Pediatr. Pulmonol.* **44,** 547–558 (2009).

655 27. Staudinger, B. J. *et al.* Conditions associated with the cystic fibrosis defect promote chronic
656 *Pseudomonas aeruginosa* infection. *Am. J. Respir. Crit. Care Med.* **189,** 812–824 (2014).

657 28. Alhede, M. *et al.* Phenotypes of non-attached *Pseudomonas aeruginosa* aggregates resemble
658 surface attached biofilm. *PLoS One* **6,** e27943 (2011).

659 29. Hall-Stoodley, L., Costerton, J. W. & Stoodley, P. Bacterial biofilms: from the natural environment
660 to infectious diseases. *Nat. Rev. Microbiol.* **2,** 95–108 (2004).

661 30. Costerton, J. W., Stewart, P. S. & Greenberg, E. P. Bacterial biofilms: a common cause of persistent
662 infections. *Science* **284,** 1318–1322 (1999).

663 31. Parsek, M. R. & Singh, P. K. Bacterial biofilms: an emerging link to disease pathogenesis. *Annu. Rev.*
664 *Microbiol.* **57,** 677–701 (2003).

665 32. Lebeaux, D., Ghigo, J. M. & Beloin, C. Biofilm-related infections: bridging the gap between clinical
666 management and fundamental aspects of recalcitrance toward antibiotics. *Microbiol. Mol. Biol.*
667 *Rev.* **78,** 510–543 (2014).

668 33. Karatan, E. & Watnick, P. Signals, regulatory networks, and materials that build and break bacterial
669 biofilms. *Microbiol. Mol. Biol. Rev.* **73,** 310–347 (2009).

670 34. Coggan, K. A. & Wolfgang, M. C. Global regulatory pathways and cross-talk control *Pseudomonas*
671 *aeruginosa* environmental lifestyle and virulence phenotype. *Curr. Issues Mol. Biol.* **14,** 47–70
672 (2012).

673 35. Jimenez, P. N. *et al.* The multiple signaling systems regulating virulence in *Pseudomonas*
674 *aeruginosa*. *Microbiol. Mol. Biol. Rev.* **76,** 46–65 (2011).

675 36. Moradali, M. F., Ghods, S. & Rehm, B. H. A. *Pseudomonas aeruginosa* Lifestyle: A Paradigm for
676 Adaptation, Survival, and Persistence. *Front. Cell. Infect. Microbiol.* **7,** 39 (2017).

677 37. Vakulskas, C. A., Potts, A. H., Babitzke, P., Ahmer, B. M. M. & Romeo, T. Regulation of bacterial
678 virulence by Csr (Rsm) systems. *Microbiol. Mol. Biol. Rev.* **79,** 193–224 (2015).

679 38. Schuster, M., Sexton, D. J., Diggle, S. P. & Greenberg, E. P. Acyl-homoserine lactone quorum sensing:
680 from evolution to application. *Annu. Rev. Microbiol.* **67,** 43–63 (2013).

681 39. Papenfort, K. & Bassler, B. L. Quorum sensing signal-response systems in Gram-negative bacteria.
682 *Nat. Rev. Microbiol.* **14,** 576–588 (2016).

683 40. Pesavento, C. & Hengge, R. Bacterial nucleotide-based second messengers. *Curr. Opin. Microbiol.*
684 **12,** 170–176 (2009).

685 41. Sajid, A., Arora, G., Singhal, A., Kalia, V. C. & Singh, Y. Protein Phosphatases of Pathogenic Bacteria:
686 Role in Physiology and Virulence. *Annu. Rev. Microbiol.* **69,** 527–547 (2015).

687 42. Römling, U., Galperin, M. Y. & Gomelsky, M. Cyclic di-GMP: the first 25 years of a universal bacterial
688 second messenger. *Microbiol. Mol. Biol. Rev.* **77,** 1–52 (2013).

689 43. Kalia, D. *et al.* Nucleotide, c-di-GMP, c-di-AMP, cGMP, cAMP, (p)ppGpp signaling in bacteria and
690 implications in pathogenesis. *Chem. Soc. Rev.* **42,** 305–341 (2013).

691 44. Stock, A. M., Robinson, V. L. & Goudreau, P. N. Two-component signal transduction. *Annu. Rev.*
692 *Biochem.* **69,** 183–215 (2000).

693 45. Porter, S. L., Wadhams, G. H. & Armitage, J. P. Signal processing in complex chemotaxis pathways.
694 *Nat. Rev. Microbiol.* **9,** 153–165 (2011).

695 46. Jung, K., Fried, L., Behr, S. & Heermann, R. Histidine kinases and response regulators in networks.

696 *Curr. Opin. Microbiol.* **15,** 118–124 (2012).

697 47. Pereira, S. F. F., Goss, L. & Dworkin, J. Eukaryote-like serine/threonine kinases and phosphatases in
698 bacteria. *Microbiol. Mol. Biol. Rev.* **75,** 192–212 (2011).

699 48. Dworkin, J. Ser/Thr phosphorylation as a regulatory mechanism in bacteria. *Curr. Opin. Microbiol.*
700 **24,** 47–52 (2015).

701 49. Pirnay, J. P. *et al. Pseudomonas aeruginosa* displays an epidemic population structure. *Environ.*
702 *Microbiol.* **4,** 898–911 (2002).

703 50. Pirnay, J. P. *et al. Pseudomonas aeruginosa* population structure revisited. *PLoS One* **4,** e7740
704 (2009).

705 51. Fazzeli, H. *et al. Pseudomonas aeruginosa* infections in patients, hospital means, and personnel's
706 specimens. *J. Res. Med. Sci.* **17,** 332–337 (2012).

707 52. Römling, U., Kader, A., Sriramulu, D. D., Simm, R. & Kronvall, G. Worldwide distribution of
708 *Pseudomonas aeruginosa* clone C strains in the aquatic environment and cystic fibrosis patients.
709 *Environ. Microbiol.* **7,** 1029–1038 (2005).

710 53. He, K. & Bauer, C. E. Chemosensory signaling systems that control bacterial survival. *Trends*
711 *Microbiol.* **22,** 389–398 (2014).

712 54. Lapouge, K., Schubert, M., Allain, F. H. & Haas, D. Gac/Rsm signal transduction pathway of gamma-
713 proteobacteria: from RNA recognition to regulation of social behaviour. *Mol. Microbiol.* **67,** 241–
714 253 (2008).

715 55. Mikkelsen, H., Sivaneson, M. & Filloux, A. Key two-component regulatory systems that control
716 biofilm formation in *Pseudomonas aeruginosa*. *Env. Microbiol.* **13,** 1666–1681 (2011).

717 56. Motley, S. T. & Lory, S. Functional characterization of a serine/threonine protein kinase of
718 *Pseudomonas aeruginosa*. *Infect. Immun.* **67,** 5386–5394 (1999).

719 57. Mougous, J. D. *et al.* A virulence locus of *Pseudomonas aeruginosa* encodes a protein secretion
720 apparatus. *Science* **312,** 1526–1530 (2006).

721 58. Mougous, J. D., Gifford, C. A., Ramsdell, T. L. & Mekalanos, J. J. Threonine phosphorylation post-
722 translationally regulates protein secretion in *Pseudomonas aeruginosa*. *Nat. Cell. Biol.* **9,** 797–803
723 (2007).

724 59. Church, D., Elsayed, S., Reid, O., Winston, B. & Lindsay, R. Burn wound infections. *Clin. Microbiol.*
725 *Rev.* **19,** 403–434 (2006).

726 60. Almagro, P. *et al. Pseudomonas aeruginosa* and mortality after hospital admission for chronic
727 obstructive pulmonary disease. *Respiration* **84,** 36–43 (2012).

728 61. Govan, J. R. & Deretic, V. Microbial pathogenesis in cystic fibrosis: mucoid *Pseudomonas aeruginosa*
729 and *Burkholderia cepacia*. *Microbiol. Rev.* **60,** 539–574 (1996).

730 62. Bjarnsholt, T. The role of bacterial biofilms in chronic infections. *APMIS Suppl*. 1–51 (2013).

731 63. Hauser, A. R., Jain, M., Bar-Meir, M. & McColley, S. A. Clinical significance of microbial infection and
732 adaptation in cystic fibrosis. *Clin. Microbiol. Rev.* **24,** 29–70 (2011).

733 64. Schleheck, D. *et al. Pseudomonas aeruginosa* PAO1 preferentially grows as aggregates in liquid
734 batch cultures and disperses upon starvation. *PLoS One* **4,** e5513 (2009).

735 65. Kirketerp-Moller, K. *et al.* Distribution, organization, and ecology of bacteria in chronic wounds. *J.*
736 *Clin. Microbiol.* **46,** 2717–2722 (2008).

737 66. Schaber, J. A. *et al. Pseudomonas aeruginosa* forms biofilms in acute infection independent of cell-
738 to-cell signaling. *Infect. Immun.* **75,** 3715–3721 (2007).

739 67. Worlitzsch, D. *et al.* Effects of reduced mucus oxygen concentration in airway Pseudomonas
740 infections of cystic fibrosis patients. *J. Clin. Invest.* **109,** 317–325 (2002).

741 68. Kragh, K. N. *et al.* Role of Multicellular Aggregates in Biofilm Formation. *MBio* **7,** e00237 (2016).

742 69. Melaugh, G. *et al.* Shaping the Growth Behaviour of Biofilms Initiated from Bacterial Aggregates.
743 *PLoS One* **11,** e0149683 (2015).

744 70. Klebensberger, J., Birkenmaier, A., Geffers, R., Kjelleberg, S. & Philipp, B. SiaA and SiaD are essential
745 for inducing autoaggregation as a specific response to detergent stress in *Pseudomonas*
746 *aeruginosa*. *Environ. Microbiol.* **11,** 3073–3086 (2009).

747 71. Klebensberger, J., Lautenschlager, K., Bressler, D., Wingender, J. & Philipp, B. Detergent-induced
748 cell aggregation in subpopulations of *Pseudomonas aeruginosa* as a preadaptive survival strategy.
749 *Environ. Microbiol.* **9,** 2247–2259 (2007).

750 72. Colley, B. *et al.* SiaA/D Interconnects c-di-GMP and RsmA signaling to coordinate cellular
751 aggregation of *Pseudomonas aeruginosa* in response to environmental conditions. *Front. Microbiol.*
752 **7,** 179 (2016).

753 73. Ravichandran, A., Sugiyama, N., Tomita, M., Swarup, S. & Ishihama, Y. Ser/Thr/Tyr
754 phosphoproteome analysis of pathogenic and non-pathogenic Pseudomonas species. *Proteomics*
755 **9,** 2764–2775 (2009).

756 74. Das, A. K., Helps, N. R., Cohen, P. T. & Barford, D. Crystal structure of the protein serine/threonine
757 phosphatase 2C at 2.0 A resolution. *EMBO J.* **15,** 6798–809 (1996).

758 75. Levdikov, V. M. *et al.* Structure of components of an intercellular channel complex in sporulating
759 *Bacillus subtilis*. *Proc. Natl. Acad. Sci.* **109,** 5441–5445 (2012).

760 76. Bradshaw, N. *et al.* A widespread family of serine/threonine protein phosphatases shares a
761 common regulatory switch with proteasomal proteases. *Elife* **6,** e26111 (2017).

762 77. Tanoue, K. *et al.* Binding of a third metal ion by the human phosphatases PP2Cα and Wip1 is
763 required for phosphatase activity. *Biochemistry* **52,** 5830–5843 (2013).

764 78. Debnath, S. *et al.* A trapped human PPM1A–phosphopeptide complex reveals structural features
765 critical for regulation of PPM protein phosphatase activity. *J. Biol. Chem.* **293,** 7993–8008 (2018).

766 79. Masuda, S. *et al.* Crystal structures of the ADP and ATP bound forms of the *Bacillus* anti-σ factor
767 SpoIIAB in complex with the anti-anti-σ SpoIIAA. *J. Mol. Biol.* **340,** 941–956 (2004).

768 80. Wang, Z. & Cole, P. A. in *Meth. Enzymol.* **548,** 1–21 (2014).

769 81. Lowe, E. D. The crystal structure of a phosphorylase kinase peptide substrate complex: kinase
770 substrate recognition. *EMBO J.* **16,** 6646–6658 (1997).

771 82. O`Neill. Tackling drug-resistant infections globally: Final report and recommendations. *Rev.*
772 *Antimicrob. Resist.* (2016). https://amr-review.org/.

773 83. Theuretzbacher, U. Global antimicrobial resistance in Gram-negative pathogens and clinical need.
774 *Curr. Opin. Microbiol.* **39,** 106–112 (2017).

775 84. Secor, P. R., Michaels, L. A., Ratjen, A., Jennings, L. K. & Singh, P. K. Entropically driven aggregation
776 of bacteria by host polymers promotes antibiotic tolerance in *Pseudomonas aeruginosa* . *Proc. Natl.*
777 *Acad. Sci.* **115,** 10780–10785 (2018).

778 85. Barraud, N., Kelso, M., Rice, S. & Kjelleberg, S. Nitric oxide: A key mediator of biofilm dispersal with
779 applications in infectious diseases. *Curr. Pharm. Des.* **21,** 31–42 (2014).

780 86. Christensen, L. D. *et al.* Synergistic antibacterial efficacy of early combination treatment with
781 tobramycin and quorum-sensing inhibitors against *Pseudomonas aeruginosa* in an intraperitoneal
782 foreign-body infection mouse model. *J. Antimicrob. Chemother.* **67,** 1198–1206 (2012).

783 87. Römling, U. & Balsalobre, C. Biofilm infections, their resilience to therapy and innovative treatment
784 strategies. *J. Intern. Med.* **272,** 541–561 (2012).

785 88. Koo, H., Allan, R. N., Howlin, R. P., Stoodley, P. & Hall-Stoodley, L. Targeting microbial biofilms:
786 current and prospective therapeutic strategies. *Nat. Rev. Microbiol.* **15,** 740–755 (2017).

787 89. Kostakioti, M., Hadjifrangiskou, M. & Hultgren, S. J. Bacterial biofilms: development, dispersal, and
788 therapeutic strategies in the dawn of the postantibiotic era. *Cold Spring Harb. Perspect. Med.* **3,**
789 a010306 (2015).

790 90. Howlin, R. P. *et al.* Low-dose nitric oxide as targeted anti-biofilm adjunctive therapy to treat chronic
791 *Pseudomonas aeruginosa* infection in cystic fibrosis. *Mol. Ther.* **25,** 2104–2116 (2017).

792 91. Jagmann, N., Henke, S. F. & Philipp, B. Cells of *Escherichia coli* are protected against severe chemical
793 stress by co-habiting cell aggregates formed by *Pseudomonas aeruginosa*. *Appl. Microbiol.*
794 *Biotechnol.* **99,** 8285–8294 (2015).

795 92. Baker, E. H. *et al.* Hyperglycaemia and pulmonary infection. *Proc. Nutr. Soc.* **65,** 227–235 (2006).

796 93. Flynn, J. M., Niccum, D., Dunitz, J. M. & Hunter, R. C. Evidence and role for bacterial mucin
797 degradation in cystic fibrosis airway disease. *PLoS Pathog.* **12,** e1005846 (2016).

798 94. LaBauve, A. E. & Wargo, M. J. Detection of host-derived sphingosine by *Pseudomonas aeruginosa*
799 is important for survival in the murine lung. *PLoS Pathog.* **10,** e1003889 (2014).

800 95. Barker, M. *et al.* Volatile organic compounds in the exhaled breath of young patients with cystic
801 fibrosis. *Eur. Respir. J.* **27,** 929–936 (2006).

802 96. Liu, Q. *et al.* 2,3-Butanediol catabolism in *Pseudomonas aeruginosa* PAO1. *Environ. Microbiol.* **20,**
803 3927–3940 (2018).

804 97. Whiteson, K. L. *et al.* Breath gas metabolites and bacterial metagenomes from cystic fibrosis
805 airways indicate active pH neutral 2,3-butanedione fermentation. *ISME J.* **8,** 1247–1258 (2014).

806 98. Nguyen, M. *et al.* The fermentation product 2,3-butanediol alters *P. aeruginosa* clearance, cytokine
807 response and the lung microbiome. *ISME J.* **10,** 2978–2983 (2016).

808 99. Venkataraman, A., Rosenbaum, M. A., Werner, J. J., Winans, S. C. & Angenent, L. T. Metabolite
809 transfer with the fermentation product 2,3-butanediol enhances virulence by *Pseudomonas*
810 *aeruginosa*. *ISME J.* **8,** 1210–1220 (2014).

811 100. Jones, C. J. *et al.* ChIP-Seq and RNA-Seq reveal an AmrZ-mediated mechanism for cyclic di-GMP
812 synthesis and biofilm development by *Pseudomonas aeruginosa*. *PLoS Pathog.* **10,** e1003984
813 (2014).

814 101. Baraquet, C. & Harwood, C. S. FleQ DNA binding consensus sequence revealed by studies of FleQ-
815 dependent regulation of biofilm gene expression in *Pseudomonas aeruginosa*. *J. Bacteriol.* **198,**
816 178–186 (2015).

817 102. Romero, M. *et al.* Genome-wide mapping of the RNA targets of the *Pseudomonas aeruginosa*
818 riboregulatory protein RsmN. *Nucleic Acids Res.* **46,** 6823–6840 (2018).

819 103. Corona, F., Reales-Calderón, J. A., Gil, C. & Martínez, J. L. The development of a new parameter for

820 tracking post-transcriptional regulation allows the detailed map of the *Pseudomonas aeruginosa*
821 Crc regulon. *Sci. Rep.* **8,** 16793 (2018).

822 104. Brencic, A. & Lory, S. Determination of the regulon and identification of novel mRNA targets of
823 *Pseudomonas aeruginosa* RsmA. *Mol. Microbiol.* **72,** 612–632 (2009).

824 105. Chew, S. C. *et al.* Matrix Polysaccharides and SiaD diguanylate cyclase alter community structure
825 and competitiveness of *Pseudomonas aeruginosa* during dual-species biofilm development with
826 *Staphylococcus aureus*. *MBio* **9,** e00585–18 (2018).

827 106. Laventie, B. J. *et al.* A Surface-induced asymmetric program promotes tissue colonization by
828 *Pseudomonas aeruginosa*. *Cell Host Microbe* **25,** 140–152.e6 (2019).

829 107. Valentini, M., Laventie, B. J., Moscoso, J., Jenal, U. & Filloux, A. The Diguanylate Cyclase HsbD
830 Intersects with the HptB Regulatory Cascade to Control *Pseudomonas aeruginosa* Biofilm and
831 Motility. *PLoS Genet.* **12,** (2016).

832 108. Baena, I. *et al.* A partner-switching system controls activation of mixed-linkage β-glucan synthesis
833 by c-di-GMP in *Sinorhizobium meliloti*. *Environ. Microbiol.* **In Press,** doi: 10.1111/1462–2920 (2019).

834 109. Ghosh, C., Sarkar, P., Issa, R. & Haldar, J. Alternatives to Conventional Antibiotics in the Era of
835 Antimicrobial Resistance. *Trends Microbiol.* **27,** 323–338 (2019).

836 110. De Smet, J., Hendrix, H., Blasdel, B. G., Danis-Wlodarczyk, K. & Lavigne, R. Pseudomonas predators:
837 Understanding and exploiting phage-host interactions. *Nat. Rev. Microbiol.* **15,** 517–530 (2017).

838 111. Pires, D. P., Cleto, S., Sillankorva, S., Azeredo, J. & Lu, T. K. Genetically Engineered Phages: a Review
839 of Advances over the Last Decade. *Microbiol. Mol. Biol. Rev.* **80,** 523–43 (2016).

840 112. Waters, E. M. *et al.* Phage therapy is highly effective against chronic lung infections with
841 *Pseudomonas aeruginosa*. *Thorax* **72,** 666–667 (2017).

842 113. Lu, T. K. & Collins, J. J. Dispersing biofilms with engineered enzymatic bacteriophage. *Proc. Natl.*
843 *Acad. Sci.* **104,** 11197–11202 (2007).

844